

# QAM-W: Joint 2D Codebook Quantization for LLM Weights via Hadamard Rotation and Activation-Aware Scaling

Preetam Sharma

Independent Research  
preetam@manifoldlab.ai

Kacper Dobek

Institute of Computing Science  
Poznan University of Technology, Poznan, Poland  
kacper.dobek@cs.put.poznan.pl

## Abstract

Scalar post-training quantizers discard pairwise coordinate structure within weight rows. We introduce QAM-W (Quadrature Amplitude Modulation for Weights), a codec that recovers this structure: each row is L2-normalized, block-Hadamard rotated, paired into 2D coordinates, and quantized against a single Lloyd-Max codebook trained on the unit circular Gaussian, with activation-aware per-channel scaling. In a cross-model study spanning five LLMs from four families (1.1B–13B parameters) and eight quantized configurations, the activation-aware variant at  $\approx 5.5$  bpw stays within  $\pm 0.4\%$  of BF16 WikiText-2 perplexity on every model, matching the SmoothQuant W8A8 quality envelope at 32% fewer weight bits. Joint 2D coding outperforms polar (amplitude  $\times$  phase) coding by 2–15 pp  $\Delta$ PPL at equal bitrate, and paired KL against BF16 tracks  $\Delta$ PPL% at Spearman  $\rho = 0.99$  across 37 (method, model) rows, consistent with a monotone composite bound from codec distortion to KL divergence. A 3.5 bpw variant is competitive on quantization-tolerant architectures. At strict 4 bpw, the rotated-codebook frontier method QTIP outperforms QAM-W; the contribution is the quality-preserving 5–6 bpw band.

## 1 Introduction

Most post-training quantizers in current use are scalar: each weight is mapped independently to a small integer index, with per-group or per-channel scales. Scalar coding is simple but leaves rate-distortion slack for sources whose coordinates are correlated. Within a weight row, coordinates are typically correlated; after an orthogonal rotation they approximate a 2D circular Gaussian. Quantizing pairs jointly – as points in the plane rather than as two independent scalars – recovers pair-level structure that a scalar codebook discards.

The empirical claim of this work is bounded: *in the  $\approx 5$ –6 bpw quality-preserving regime,*

an activation-aware joint-2D codec stays within  $\pm 0.4\%$  of BF16 perplexity across five LLMs from four families spanning 1.1B–13B parameters, matching SmoothQuant (Xiao et al., 2023) W8A8’s quality at  $\approx 32\%$  fewer *weight* bits. At strict 4 bpw, QTIP (Tseng et al., 2024b) outperforms QAM-W (section 5.2); the contribution here is the 5–6 bpw band.

Rotation-based methods such as QuIP (Chee et al., 2023) and QuIP# (Tseng et al., 2024a) apply incoherent rotations to homogenize coordinate magnitudes before scalar or lattice coding. Activation-aware methods such as AWQ (Lin et al., 2024) exploit the per-channel activation scale but leave joint coordinate structure untouched. The codec presented here combines all three ideas: a deterministic block-Hadamard rotation, joint 2D Lloyd-Max coding against a single codebook trained on the unit circular Gaussian (Lloyd, 1982), and AWQ-style per-channel scaling driven by the layer-output trace identity.

Throughout, reported bits-per-weight (bpw) refers to weight-storage and memory-bandwidth footprint. The current pipeline dequantizes to BF16 before matmul; latency claims would require a fused kernel and are out of scope (see section 6).

## Contributions:

- **Codec and analysis.** A row-norm-factored, block-Hadamard-rotated, joint 2D Lloyd-Max codec for LLM weights with activation-aware scaling, backed by a composite monotone bound from codec distortion to KL divergence (sections 3 and 4).
- **Cross-model study.** Eight quantized configurations on five LLMs under a unified perplexity, paired-KL, and six-task harness protocol (sections 5.1 and 5.2).
- **KL as rank diagnostic.** Across 37 (method,

model) rows, paired KL and  $\Delta\text{PPL}\%$  are rank-correlated at Spearman  $\rho = 0.99$ .

## 2 Related Work

**Scalar post-training quantization.** Round-to-nearest (RTN) quantization (Krishnamoorthi, 2018) with per-group scaling is the simplest baseline. GPTQ (Frantar et al., 2023) compensates quantization error column-by-column using approximate second-order information. AWQ (Lin et al., 2024) protects high-activation channels via per-channel scaling; AutoRound (Cheng et al., 2023) refines rounding with SignSGD; HQQ (Badri and Shaji, 2023) treats rounding as a half-quadratic problem without calibration data. SmoothQuant (Xiao et al., 2023) redistributes quantization difficulty from activations to weights through a diagonal scaling transform, targeting joint W8A8. OmniQuant (Shao et al., 2024) jointly learns clipping and smoothing transforms. LLM.int8() (Dettmers et al., 2022) keeps outlier activation channels in 16-bit mixed precision. SqueezeLLM (Kim et al., 2024) couples a non-uniform scalar codebook with a dense-and-sparse decomposition; QLoRA’s NF4 (Dettmers et al., 2023) places levels on the Gaussian distribution.

**Rotated and vector quantization.** QuIP (Chee et al., 2023) and QuIP# (Tseng et al., 2024a) apply random or structured orthogonal rotations to decorrelate weight coordinates before quantization. QuaRot (Ashkboos et al., 2024) extends rotation through the residual stream for end-to-end 4-bit inference; SpinQuant (Liu et al., 2025) replaces the fixed rotation with a learned one. QAM-W shares the rotation principle but opts for a deterministic block-Hadamard, which requires no calibration on the rotation itself. Iso-bpw comparison against the learned-rotation family is deferred to future work.

On the VQ side, AQLM (Egiazarian et al., 2024) uses additive codebooks and pushes below 2.5 bpw. QTIP (Tseng et al., 2024b) combines an  $E_8$ -lattice trellis with Hadamard incoherence and is the strongest published rotated-codebook method; it and QAM-W occupy different operating points, with QTIP stronger at strict 4 bpw and QAM-W stronger in the 5–6 bpw band (section 5.2). VPTQ (Liu et al., 2024) stacks residual codebooks down to  $\sim 2$  bpw; GPTVQ (van Baalen et al., 2024) shows the rate-distortion gain from higher codebook dimension saturates around  $d=8$ , placing QAM-W’s  $d=2$  choice at the small end of

that spectrum by design.

**Concurrent work.** PolarQuant (Vicentino, 2026) couples a Walsh-Hadamard rotation with a *scalar* ( $d=1$ ) Lloyd-Max codebook, sharing QAM-W’s first two pipeline stages but differing in codebook dimension. The  $d=1$  vs.  $d=2$  ablation is the highest-priority follow-up.

**Signal-processing origins.** Quadrature amplitude modulation (QAM) originates in digital communications (Proakis and Salehi, 2008); QAM-W adapts this geometric view to weight compression. The codebook training follows the Lloyd-Max tradition (Lloyd, 1982; Max, 1960) extended to 2D sources, and can be seen as a Hadamard-rotated generalization of the  $k$ -means weight clustering in Deep Compression (Han et al., 2016).

## 3 QAM-W Codec Pipeline

This section describes the codec as an encoder/decoder pair. The mathematical properties of the rotation and polar baseline are separated into section A.

### 3.1 Encoder

QAM-W quantizes a weight matrix  $W \in \mathbb{R}^{d_{\text{out}} \times d_{\text{in}}}$  row-by-row. For each row  $w$ , the encoder performs the following steps:

1. **Separate scale from direction.** Record the row norm  $r = \|w\|_2$  as separate metadata and normalize the row to  $u = w/r$  when  $r > 0$ . If  $r = 0$ , the row is encoded as a zero row.
2. **Rotate the direction.** Apply a deterministic sign-masked block-Hadamard rotation, giving  $y = R_{\text{fwd}}u$ .
3. **Pair coordinates.** Group adjacent rotated coordinates into complex values  $z_k = y_{2k} + iy_{2k+1}$  for  $k = 0, \dots, d/2 - 1$ .
4. **Normalize each pair.** Divide each pair by its calibrated scale  $\sigma_k$ .
5. **Quantize.** Encode each normalized pair either with the polar baseline codebooks or with the joint 2D QAM-W codebook.
6. **Pack.** Store the resulting codebook indices in a bit-packed byte stream.

### 3.2 Decoder

The decoder reverses the encoder: unpack codebook indices, look up the corresponding centroids, rescale each pair by  $\sigma_k$ , reassemble pairs into a rotated real vector, apply the inverse rotation  $R_{\text{inv}}$ , and multiply by the stored row norm  $r$ . The benchmark charges 16 bits per row for norm metadata; a fully serialized f16 row norm would add a small radial quantization term not part of the directional analysis in section A.

### 3.3 Rotation Choice

The rotation used by the encoder is a block-Hadamard transform with a deterministic sign mask. It is cheap to apply with a butterfly algorithm and requires no stored dense matrix. The implementation chooses the block size  $b$  as the largest power of two dividing the row dimension  $d_{\text{in}}$ , capped at  $b_{\text{max}} = 1024$ . For the weight matrices in the experiments in this paper,  $d_{\text{in}} = 2048$  uses  $b = 1024$  and  $d_{\text{in}} = 5632$  uses  $b = 512$ . The rotation’s exact isometry property is proved in lemma 1.

### 3.4 Pair Calibration

After rotation, adjacent coordinates are modeled empirically as approximately circular Gaussian pairs with pair-specific scale  $\sigma_k$ . Under the idealized model that the two coordinates in pair  $k$  are zero-mean Gaussian variables with equal variance  $\sigma_k^2$  and zero covariance, the amplitude  $|z_k|$  is Rayleigh distributed and  $\mathbb{E}|z_k| = \sigma_k \sqrt{\pi/2}$ . Calibration therefore estimates

$$\hat{\sigma}_k = \frac{\text{mean}(|z_k|)}{\sqrt{\pi/2}} \quad (1)$$

from up to 1024 unit-normalized rows per weight matrix.

### 3.5 Polar Baseline

The polar baseline quantizes amplitude and phase independently. The amplitude  $|z_k|/\sigma_k$  is quantized with an  $N_a = 2^{B_a}$  level Lloyd-Max codebook for the unit Rayleigh density  $f(r) = re^{-r^2/2}$ . The phase  $\arg(z_k)$  is rounded to one of  $N_p = 2^{B_p}$  uniform bins. The total per-pair budget is  $B = B_a + B_p$  bits. The pairwise distortion model for this baseline is analyzed in theorem 1.

### 3.6 Joint 2D QAM

The main QAM-W variant replaces the two independent polar codebooks with a single 2D code-

book  $\mathcal{C} = \{c_0, \dots, c_{2^B-1}\} \subset \mathbb{R}^2$ . The codebook is trained by Lloyd iterations on the unit circular Gaussian

$$f(x, y) = \frac{1}{2\pi} \exp\left(-\frac{x^2 + y^2}{2}\right). \quad (2)$$

Encoding maps each normalized pair  $z_k/\sigma_k$  to its nearest codebook entry by Euclidean distance. Decoding is a table lookup followed by multiplication by  $\sigma_k$ .

The current experiments use  $B = 11$  bits per pair, matching the 5+6 polar configuration in nominal pair payload. Native byte alignment and stream layout can differ between polar and joint-2D implementations; the comparison is therefore equal-bits-per-pair rather than byte-identical storage.

The choice  $d = 2$  is also deliberate at the decode end: reconstruction is a single lookup into a  $2^B$ -entry table that, at  $B \leq 11$ , occupies at most 16 KB and stays L1-resident. This is structurally simpler than the multi-codebook lookups and vector additions of additive methods such as AQLM (Egiazarian et al., 2024), or the sequential trellis decoding of QTIP (Tseng et al., 2024b). Given that rate-distortion gains saturate by  $d \approx 8$  (section 2),  $d = 2$  deliberately trades part of the asymptotic ceiling for a decode path that is one cache-resident table read.

### 3.7 Bitrate Accounting

The bitrate per weight includes  $B$  bits per pair for the codebook index and 16 bits per row for row-norm metadata. Since each pair covers two scalar coordinates,

$$\text{bpw} = \frac{B}{2} + \frac{16}{d_{\text{in}}}. \quad (3)$$

For  $d_{\text{in}} = 2048$  and  $B = 11$ , this is approximately 5.51 bpw before byte-alignment overhead. Reported bitrates include the row-level packing and alignment used by the implementation.

### 3.8 The QAM-W-3.5 Low-Bit Variant

To probe the sub-4 bpw regime, QAM-W is instantiated with  $B = 7$  bits per pair, giving a  $2^7 = 128$ -entry 2D Lloyd-Max codebook trained on the same unit circular Gaussian. Activation-aware per-channel scaling (section B) remains applicable. For  $d_{\text{in}} = 2048$  the per-pair budget plus row-norm metadata gives  $\text{bpw} \approx 3.51$ ; the AWQ-aware variant adds  $\sim 0.003$  bpw of per-channel scale metadata for  $\alpha = 0.3$ . This is the configuration analyzed in section 5.3.1.

## 4 Analysis

QAM-W’s design rests on four analytical results. We state them here and defer the formal statements, proofs, and supporting empirical checks to sections A to C.

**The rotation is distortion-free.** The sign-masked block-Hadamard rotation is an exact isometry in real arithmetic (lemma 1): it adds no reconstruction error and only redistributes energy within each block before quantization. It does not by itself make the rotated coordinates Gaussian; that the post-rotation complex pairs concentrate near a circular Gaussian is an empirical property, checked by QQ plots against fitted Rayleigh and Gaussian marginals (section A.4).

**Joint 2D coding dominates polar at fixed rate.** For the polar baseline, the per-pair distortion splits into an amplitude term and a phase term with a closed form under the Rayleigh–Lloyd source model (theorem 1 and corollary 1). Because that factorization codes amplitude and phase independently, it cannot capture the pair-level correlation that a single 2D codebook exploits.

**Activation-weighted error is the right objective.** The layer-output error obeys the trace identity  $\|X\Delta W^\top\|_F^2 = \text{Tr}(\Delta W \hat{M}_x \Delta W^\top)$  (proposition B.1), so what a quantized layer actually contributes is *activation-weighted* error, not raw weight MSE. This motivates AWQ-style per-channel scaling, which attenuates the contribution of high-RMS input channels under a diagonal- $M_x$  model (corollary 3 and proposition B.2). Empirically, the amplification of weight-domain Frobenius error into layer-output RMSE varies by  $0.55\text{--}5.5\times$  across layers and methods (table 4).

**A monotone codec-to-KL bound.** Chaining the rotation isometry, the pairwise identity, the layer-output trace identity, and a softmax-Fisher local KL expansion (corollary 4) yields an upper bound on the paired KL between the BF16 and quantized models that is monotone in two scalars: the per-pair Lloyd distortion  $D_B$  (codec) and a model-fixed constant  $C_W$  (theorem 2). The bound motivates, but does not prove, that realized KL should rank methods the same way  $D_B$  does; across the 37 (method, model) rows in this study, paired KL and  $\Delta\text{PPL}\%$  are rank-correlated at Spearman  $\rho = 0.99$  (fig. 1).

## 5 Experiments

Eight quantized configurations are evaluated against a BF16 reference on three instruction-tuned LLMs: TinyLlama-1.1B-Chat (Zhang et al., 2024), Qwen2.5-3B-Instruct (Yang et al., 2024), and Mistral-7B-Instruct-v0.3 (Jiang et al., 2023). These are dense decoder-only transformers with standard attention, chosen so the comparison rests on mature, audited loading and evaluation tooling (see Limitations). Only MLP gate, up, and down projections are quantized; attention weights and the LM head remain BF16.

**Baselines.** Five external methods: RTN (Krishnamoorthi, 2018), GPTQ (Frantar et al., 2023), AWQ (Lin et al., 2024), and AutoRound (Cheng et al., 2023), all at W4A16 g128 ( $\approx 4.1$  bpw); SmoothQuant (Xiao et al., 2023) W8A8 ( $\approx 8.1$  bpw). *SmoothQuant eval mode*: weights are smoothed and fake-quantized to int8 then restored to BF16; activations stay BF16. All comparisons against SmoothQuant in this paper are on weight storage and memory bandwidth, not matmul arithmetic.

**QAM-W variants.** QAM-W-polar (polar baseline,  $\approx 4.0$  bpw), QAM-W-4 (joint 2D,  $B = 8$ ,  $\approx 4.0$  bpw), and QAM-W-5.5 (joint 2D,  $B = 11$ , AWQ-style scaling  $\alpha = 0.3$ ,  $\approx 5.5$  bpw). A sub-4 bpw variant QAM-W-3.5 ( $B = 7$ ,  $\approx 3.5$  bpw) is reported in section 5.3.1.

**Metrics.** WikiText-2 (Merity et al., 2017) stride perplexity (seq\_len 2048, stride 1024, 16K scored tokens); paired KL divergence against BF16 (4K scored tokens); six-task lm-evaluation-harness (Gao et al., 2024) panel (PIQA (Bisk et al., 2020), HellaSwag (Zellers et al., 2019), COPA (Roemmele et al., 2011), RTE (Wang et al., 2018), OpenBookQA (Mihaylov et al., 2018), LAMBADA-OpenAI (Paperno et al., 2016)). Full reproducibility details including model SHAs, calibration setup, and hardware are in section J.

### 5.1 Cross-Model Quality Results

Table 1 summarizes the cross-model quality story.

**QAM-W-5.5 reaches the BF16 envelope at the lowest bitrate.** At  $\approx 5.5$  bpw, QAM-W-5.5 stays within  $\pm 0.4\%$  of BF16 perplexity on all three models. SmoothQuant W8A8 reaches the same envelope but at  $\approx 8.1$  bpw — about 47% more weight bits.

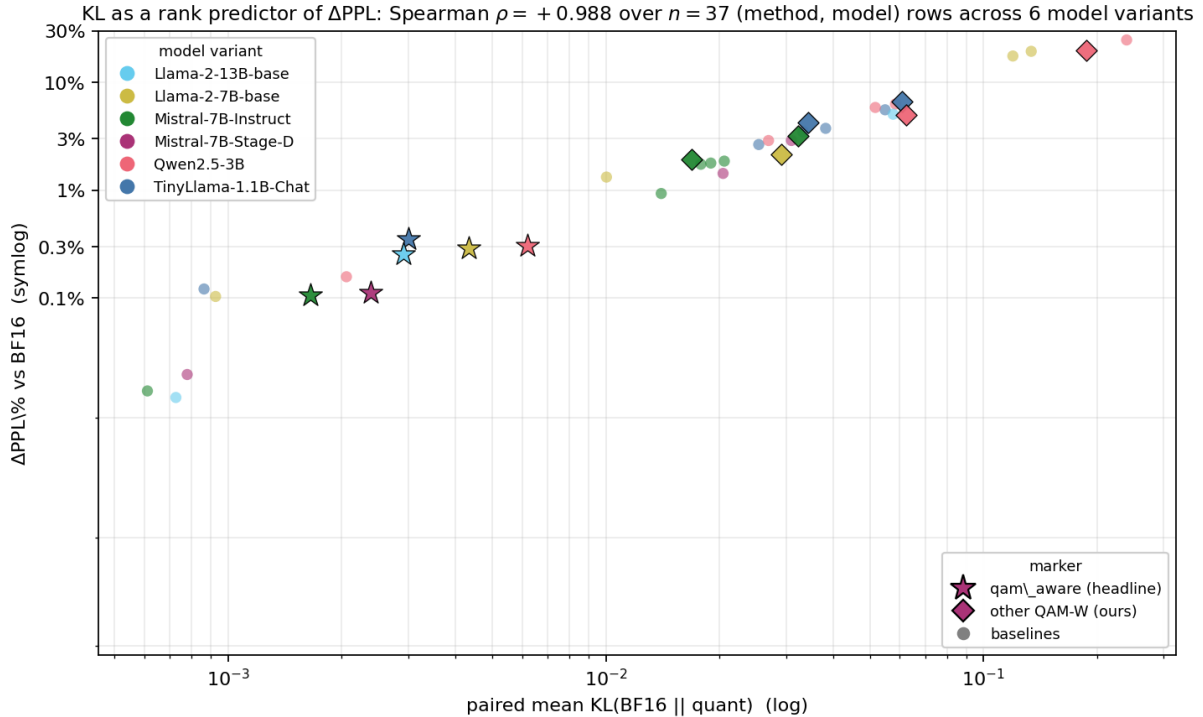


Figure 1: Empirical check of theorem 2: measured paired KL ( $\log x$ ) vs. measured  $\Delta$ PPL% (symlog  $y$ ) for every (method, model) row. Only the headline points and the two large outlier points are labelled to avoid clutter. The pooled rank correlation across all 37 (method, model) rows spanning six model variants is Spearman  $\rho = 0.99$ .

### Calibration narrows the cross-model spread.

Uncalibrated RTN costs +1.9% on Mistral 7B but +24.6% on Qwen 2.5 3B — a  $12\times$  spread driven by architecture alone. Among calibrated methods (GPTQ, AWQ, AutoRound, QAM-W-5.5) the cross-model spread is much tighter. Single-model comparisons among uncalibrated quantizers can therefore mislead in a way that calibrated comparisons typically do not.

### Joint 2D coding beats polar at equal bitrate.

At  $\approx 4$  bpw, QAM-W-4 beats QAM-W-polar by 1–3 pp of  $\Delta$ PPL on the quantization-tolerant models (TinyLlama, Mistral) and by 14.6 pp on the quantization-sensitive Qwen 2.5. The joint codebook captures pair-level correlations that the polar factorization discards; the gain is largest precisely where the model is most sensitive to codec choice.

#### 5.1.1 Cross-Model Slope

Across the 37 (method, model) rows assembled in this study, paired KL and  $\Delta$ PPL% are rank-correlated at Spearman  $\rho = 0.99$  (fig. 1), consistent with the composite bound in section 4. Multi-seed stride-offset rescaling confirms the ranking is robust (std 0.03–0.08 pp; section G).

## 5.2 Iso-bpw Frontier Comparison

To position QAM-W against the rotated-codebook frontier, we run an iso-bpw comparison on Llama-2-7B-base (Touvron et al., 2023) against QTIP (Tseng et al., 2024b) (4-bit and 2-bit) and AQLM (Egiazarian et al., 2024) (2-bit), using published HuggingFace checkpoints dequantized to BF16 before scoring under our protocol.

### QAM-W-5.5 transfers; QTIP leads at 4 bpw.

QAM-W-5.5 on Llama-2-7B-base reaches +0.29%  $\Delta$ PPL, within the same envelope as the cross-model rows. At iso-4-bpw, QTIP-4Bit (+1.32%, KL 0.010) beats QAM-W-4 (+2.15%, KL 0.029): QTIP’s  $E_8$  lattice trellis and BlockLDLQ rounding outpace QAM-W’s  $d = 2$  Lloyd codebook at a strict 4-bit ceiling. QAM-W-5.5 improves over QTIP-4Bit only at  $\sim 1.4\times$  the bit budget — a different operating point, not a Pareto win.

**Low-bpw frontier.** At  $\approx 2$  bpw, QTIP and AQLM take comparable PPL hits (+17–19%). QAM-W has no 2-bpw operating point; its closest variant is QAM-W-3.5 at  $\approx 3.5$  bpw (section 5.3.1).

Table 1: Cross-architecture quantization sensitivity. Each column reports  $\Delta\text{PPL}\%$  versus that model’s BF16 reference (anchor PPL in the column header); rows are sorted by ascending mean  $\Delta$  across models. QAM-W-5.5 is the lowest-bpw method in the BF16-quality envelope: the only sub-8 bpw method that stays within  $\pm 0.4\%$  of BF16 on every model. Detailed per-model breakdowns with paired KL and harness average are in section H. *Reader key:*  $\downarrow$  lower is better. Shaded rows ( $\star$ ) mark QAM-W (ours).

method	bpw $\downarrow$	TinyLlama-1.1B $\Delta$ vs 7.1499 $\downarrow$	Qwen2.5-3B $\Delta$ vs 6.7826 $\downarrow$	Mistral-7B $\Delta$ vs 4.8883 $\downarrow$
SmoothQuant W8A8	8.1	+0.1%	+0.2%	+0.0%
$\star$ QAM-W-5.5	5.5	+0.4%	+0.3%	+0.1%
GPTQ W4A16 g128	4.1	+2.6%	+2.9%	+0.9%
AutoRound W4A16 g128	4.1	+3.5%	+5.8%	+1.7%
AWQ W4A16 g128	4.1	+3.7%	+6.3%	+1.8%
$\star$ QAM-W-4	4.0	+4.2%	+5.0%	+1.9%
RTN W4A16 g128	4.1	+5.6%	+24.6%	+1.9%
$\star$ QAM-W-polar	4.0	+6.6%	+19.6%	+3.2%

Table 2: Frontier comparison on Llama-2-7B-base, sorted by ascending bpw. SmoothQuant W8A8 bpw is over MLP weights only; QTIP, AQLM, and the QAM-W rows quantize the full weight pool per their published configurations. *Reader key:*  $\downarrow$  lower is better,  $\uparrow$  higher is better. Shaded rows ( $\star$ ) are QAM-W (ours).

config	bpw $\downarrow$	PPL $\downarrow$	$\Delta\text{PPL}\%$ $\downarrow$	mean KL $\downarrow$	harness avg $\uparrow$
BF16 (ref)	16.00	4.7527	—	—	0.6990
SmoothQuant W8A8	8.13	4.7576	+0.10%	0.0009	0.7009
$\star$ QAM-W-5.5	5.51	4.7664	+0.29%	0.0043	0.7008
QTIP 4-bit (relaxml)	4.00	4.8155	+1.32%	0.0100	0.7027
$\star$ QAM-W-4	4.00	4.8551	+2.15%	0.0292	0.6993
QTIP 2-bit (relaxml)	2.00	5.5841	+17.49%	0.1195	0.6764
AQLM 2-bit $1\times 16$ (ISTA-DASLab)	2.03	5.6716	+19.33%	0.1337	0.6782

### 5.3 Operating Points and Downstream Behavior

#### 5.3.1 Low-Bit Operating Point: QAM-W-3.5

A  $B=7$  codebook (128 codewords) drops QAM-W to  $\approx 3.5$  bpw. On TinyLlama, activation-aware scaling recovers  $\approx 0.5$  bits of effective precision: QAM-W-3.5 (+4.1%  $\Delta\text{PPL}$ , KL 0.037) essentially ties the unscaled QAM-W-4 at 4.0 bpw (+4.2%, KL 0.034). Without scaling the 7-bit codec costs +7.6%. On Qwen 2.5 the 128-entry codec is not yet Pareto-competitive (+7.5%, worse than GPTQ (Frantar et al., 2023) at +2.9%), indicating  $\sim 4$  bpw as the lower bound at which the 2D codec geometry pays off on sensitive architectures. On Mistral 7B, 3.5 bpw costs only +1.98%. Full results in section E.

#### 5.3.2 Downstream Task Behavior

A six-task lm-evaluation-harness (Gao et al., 2024) panel corroborates the PPL story. LAMBADA is the most quantization-sensitive task; PIQA (Bisk

et al., 2020) and COPA (Roemmele et al., 2011) are nearly flat across methods within each model; per-task 95% CI is  $\pm 2-3$  pp at the evaluation limits used, so within-model cross-method differences inside that interval should be read as ties. Per-task breakdowns and Pareto plots are in section H.

**MMLU.** QAM-W-5.5 and BF16 scored on the full 57-subject MMLU (Hendrycks et al., 2021) panel match within 0.2 pp on all three models (table 3), confirming the codec’s quality envelope extends beyond the perplexity metric.

## 6 Conclusion

The activation-aware joint-2D variant of QAM-W reaches the BF16 quality envelope at  $\approx 5.5$  bpw on all five models tested, with  $\Delta\text{PPL} \leq 0.4\%$  on each. Three assumptions underpin the codec: (i) weight-row coordinates are correlated and admit a homogenizing orthogonal rotation; (ii) the rotated pairs concentrate near a circular Gaussian suitable for

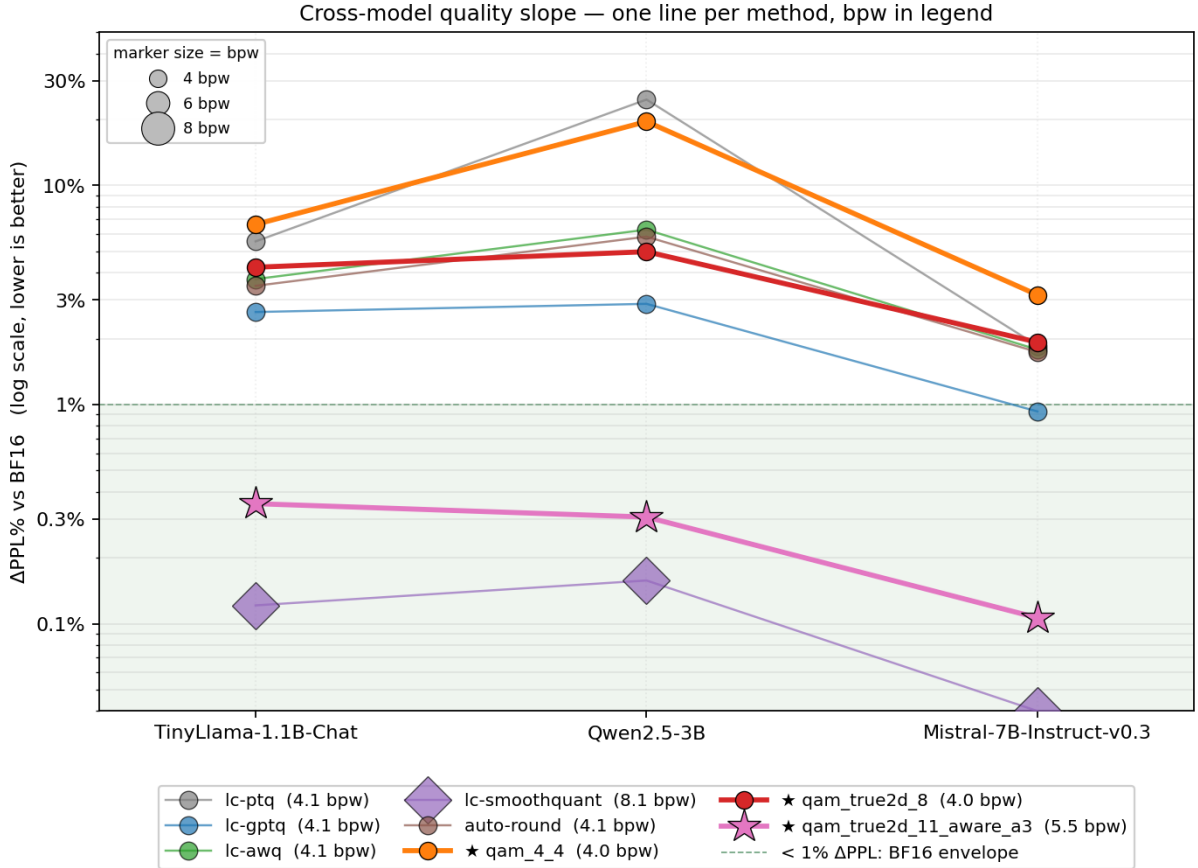


Figure 2: Cross-model  $\Delta\text{PPL}\%$  slope. One line per method; the shaded band at the bottom is the  $< 1\%$  BF16-envelope zone. Two methods are drawn thicker as the headline: QAM-W-5.5 ( $\star$ ,  $\approx 5.5$  bpw) sits inside the envelope on all three architectures; SmoothQuant ( $\diamond$ ,  $\approx 8.1$  bpw) reaches the same envelope but at  $\sim 47\%$  higher bitrate.

Table 3: MMLU macro-average accuracy (57 subjects, limit=300). QAM-W-5.5 matches BF16 within 0.2 pp on all three models. *Reader key*:  $\uparrow$  higher is better.

model	BF16 $\uparrow$	QAM-W-5.5 $\uparrow$	$\Delta$ (pp)
TinyLlama-1.1B	0.2489	0.2507	+0.18
Qwen2.5-3B	0.6700	0.6685	-0.15
Mistral-7B	0.6150	0.6153	+0.03

joint 2D Lloyd coding; (iii) per-channel activation magnitudes provide a rescaling that aligns codec error with the low-eigenvalue directions of  $M_x$ . When any of these weakens — as on Qwen 2.5 3B — all three are needed to recover quality.

In practice, QAM-W-5.5 ( $\approx 5.5$  bpw) is the quality-preserving choice, matching SmoothQuant (Xiao et al., 2023) W8A8 at  $\approx 32\%$  fewer weight bits. QAM-W-4 ( $\approx 4$  bpw) serves as the iso-bitrate comparison against W4A16 baselines and directly demonstrates that joint 2D coding outperforms polar by 1–3 pp on

quantization-tolerant models and by over 14 pp on the most quantization-sensitive one. QAM-W-3.5 ( $\approx 3.5$  bpw) is viable on quantization-tolerant architectures but not yet Pareto-competitive on sensitive ones.

More broadly, among uncalibrated quantizers, sensitivity is dominated by the model architecture: RTN costs +1.9% on Mistral but +24.6% on Qwen, a  $12\times$  difference from changing the model alone. Among calibrated methods, the spread is much smaller. Single-model comparisons can therefore mislead. Natural follow-ups include a learned 2D codebook fit to each checkpoint’s empirical pair distribution and a fused dequantization-matmul kernel to translate the bitrate saving into inference latency gains.

## Limitations

**Scope of quantized parameters.** The cross-model headline tables (section 5.1) report bpw over MLP gate/up/down projections only; attention weights and the LM head remain BF16. The

MLP + attention extension in section F.1 adds the four self-attention projections ( $q, k, v, o$ ) for the BF16 reference and the four strongest sub-8 bpw quantized methods on Mistral 7B and shows the ranking is preserved, but the cross-model tables themselves do not yet include an MLP + attention row for TinyLlama and Qwen; the LM head remains untouched in every reported configuration.

**Codebook training cost.** Lloyd-Max codebook training for the joint 2D codec is a one-time cost of  $\sim 5$  s per bitrate level. This is negligible compared to inference, but it is non-zero and is performed on a synthetic unit circular Gaussian rather than per-checkpoint — a learned codebook conditioned on the empirical post-rotation pair distribution might buy additional precision.

**Activation-aware  $\alpha$  is grid-tuned, not learned.** The AWQ-style per-channel scaling exponent  $\alpha = 0.3$  was chosen from a small grid  $\{0.0, 0.3, 0.5, 0.8\}$  on TinyLlama and held fixed across models. A per-model or per-layer  $\alpha$  schedule would likely improve quality on Qwen 2.5, where the 7-bit codec is most  $\alpha$ -sensitive.

**Architecture coverage.** The cross-model tables rest on three instruction-tuned models from three families (TinyLlama, Qwen 2.5, Mistral) plus two Llama-2 base models at 7B and 13B (sections 5.2 and F.2) — five models from four families across 1.1B–13B parameters. Beyond this range, 70B and contemporary families (Llama 3, Gemma 2, DeepSeek) would further tighten the architecture-sensitivity claim, particularly to test whether the  $\approx 5.5$  bpw envelope continues to hold at the 70B parameter scale where activation statistics diverge further from the smaller-model distributions calibrated against here. The choice to evaluate on these architecturally conventional models is deliberate: all five are dense decoder-only transformers with standard multi-head or grouped-query attention, for which mature weight-loading and evaluation libraries make the codec comparison free of model-loading confounds. Contemporary (2026-era) architectures are not yet reliably supported end-to-end by stock libraries — e.g. Gemma-4 combines per-layer input embeddings with interleaved local/global sliding-window attention and must be loaded through a forked model implementation. Extending QAM-W to such architectures, via a dedicated inference engine, is left to future work.

**Iso-4-bpw quality trails the QTIP frontier.** Section 5.2 reports QTIP-4Bit ahead of QAM-W’s joint-2D codec at iso-4-bpw on Llama-2-7B-base; the joint-2D Lloyd codebook trades some rate-distortion ceiling for training cheapness and decode simplicity (a single  $2^B$ -entry table lookup rather than a lattice nearest-point search). Closing the iso-4-bpw gap is the most natural extension: candidate paths are a richer codebook training distribution per checkpoint (section 6) and tighter Lloyd optimization with QTIP-style BlockLDLQ rounding.

**Harness precision.** The six-task harness panel uses `limit=300` (Qwen, Mistral) and `limit=500` (TinyLlama). The resulting per-task accuracy noise floor is on the order of one to two percentage points; cross-method differences smaller than that should be read as ties.

**No fused dequantization-matmul kernel.** The reported bpw is a storage metric. The current pipeline dequantizes weights to BF16 before the linear-layer matmul, so the bitrate saving shows up in weight storage and host-to-device memory bandwidth, not in matmul arithmetic. The bpw numbers should be read as memory-footprint claims until a fused kernel is available. Building this kernel — and with it support for architectures beyond the conventional dense transformers studied here — is the primary engineering follow-up.

**Comparison scope.** The evaluation covers five models from four families and seven baselines under one unified protocol. Notably absent are iso-bpw comparisons against learned-rotation methods (QuaRot, SpinQuant) and a direct  $d=1$  vs.  $d=2$  ablation against PolarQuant (Vicentino, 2026), which would isolate the codebook-dimension contribution from the shared rotation-plus-scaling pipeline. Scale beyond 13B and broader downstream benchmarks (MMLU-Pro, BBH, IFEval, GSM8K) are also not covered.

## References

- Saleh Ashkboos, Amirkeivan Mohtashami, Maximilian L Croci, Bo Li, Pashmina Cameron, Martin Jaggi, Dan Alistarh, Torsten Hoefler, and James Hensman. 2024. QuaRot: Outlier-free 4-bit inference in rotated LLMs. In *Advances in Neural Information Processing Systems (NeurIPS)*.
- Hicham Badri and Appu Shaji. 2023. Half-quadratic quantization of large machine learning models. [https://mobiusml.github.io/hq\\_blog/](https://mobiusml.github.io/hq_blog/).

- Yonatan Bisk, Rowan Zellers, Ronan Le Bras, Jianfeng Gao, and Yejin Choi. 2020. PIQA: Reasoning about physical commonsense in natural language. In *AAAI Conference on Artificial Intelligence*.
- Jerry Chee, Yaohui Cai, Volodymyr Kuleshov, and Christopher De Sa. 2023. Quip: 2-bit quantization of large language models with guarantees. In *Advances in Neural Information Processing Systems (NeurIPS)*.
- Wenhua Cheng, Weiwei Zhang, Haihao Shen, Yiyang Cai, Xin He, and Kaokao Lv. 2023. Optimize weight rounding via signed gradient descent for the quantization of llms. *arXiv preprint arXiv:2309.05516*.
- Tim Dettmers, Mike Lewis, Younes Belkada, and Luke Zettlemoyer. 2022. LLM.int8(): 8-bit matrix multiplication for transformers at scale. In *Advances in Neural Information Processing Systems (NeurIPS)*.
- Tim Dettmers, Artidoro Pagnoni, Ari Holtzman, and Luke Zettlemoyer. 2023. Qlora: Efficient finetuning of quantized llms. In *Advances in Neural Information Processing Systems (NeurIPS)*.
- Vage Egiazarian, Andrei Panferov, Denis Kuznedelev, Elias Frantar, Artem Babenko, and Dan Alistarh. 2024. Extreme compression of large language models via additive quantization. In *Proceedings of the 41st International Conference on Machine Learning (ICML)*.
- Elias Frantar, Saleh Ashkboos, Torsten Hoefler, and Dan Alistarh. 2023. GPTQ: Accurate post-training quantization for generative pre-trained transformers. In *International Conference on Learning Representations (ICLR)*.
- Leo Gao, Jonathan Tow, Baber Abbasi, Stella Biderman, Sid Black, Anthony DiPofi, Charles Foster, Laurence Golding, Jeffrey Hsu, Alain Le Noac’h, Haonan Li, Kyle McDonell, Niklas Muennighoff, Chris Ociepa, Jason Phang, Laria Reynolds, Hailey Schoelkopf, Aviya Skowron, Lintang Sutawika, and 5 others. 2024. [A framework for few-shot language model evaluation \(lm-evaluation-harness\)](#). Zenodo, version 0.4.x.
- Allen Gersho and Robert M Gray. 1991. *Vector Quantization and Signal Compression*. Kluwer Academic Publishers.
- Song Han, Huizi Mao, and William J Dally. 2016. Deep compression: Compressing deep neural networks with pruning, trained quantization and Huffman coding. In *International Conference on Learning Representations (ICLR)*.
- Dan Hendrycks, Collin Burns, Steven Basart, Andy Zou, Mantas Mazeika, Dawn Song, and Jacob Steinhardt. 2021. Measuring massive multitask language understanding. In *ICLR*.
- Albert Q Jiang, Alexandre Sablayrolles, Arthur Mensch, Chris Bamford, Devendra Singh Chaplot, Diego de las Casas, Florian Bressand, Gianna Lengyel, Guillaume Lample, Lucile Saulnier, L lio Renard Lavaud, Marie-Anne Lachaux, Pierre Stock, Teven Le Scao, Thibaut Lavril, Thomas Wang, Timoth e Lacroix, and William El Sayed. 2023. Mistral 7B. *arXiv preprint arXiv:2310.06825*.
- Sehoon Kim, Coleman Hooper, Amir Gholami, Zhen Dong, Xiuyu Li, Sheng Shen, Michael W Mahoney, and Kurt Keutzer. 2024. SqueezeLLM: Dense-and-sparse quantization. In *Proceedings of the 41st International Conference on Machine Learning (ICML)*.
- Raghuraman Krishnamoorthi. 2018. [Quantizing deep convolutional networks for efficient inference: A whitepaper](#). Preprint, arXiv:1806.08342.
- Ji Lin, Jiaming Tang, Haotian Tang, Shang Yang, Weiming Chen, Wei-Chen Wang, Guangxuan Xiao, Xingyu Dang, Chuang Gan, and Song Han. 2024. AWQ: Activation-aware weight quantization for LLM compression and acceleration. In *Proceedings of Machine Learning and Systems (MLSys)*. Best Paper Award.
- Yifei Liu, Jicheng Wen, Yang Wang, Shengyu Ye, Li Lyna Zhang, Ting Cao, Cheng Li, and Mao Yang. 2024. VPTQ: Extreme low-bit vector post-training quantization for large language models. In *Empirical Methods in Natural Language Processing (EMNLP)*.
- Zechun Liu, Changsheng Zhao, Igor Fedorov, Bilge Soran, Dhruv Choudhary, Raghuraman Krishnamoorthi, Vikas Chandra, Yuandong Tian, and Tijmen Blankevoort. 2025. SpinQuant: LLM quantization with learned rotations. In *International Conference on Learning Representations (ICLR)*.
- Stuart P Lloyd. 1982. Least squares quantization in pcm. *IEEE Transactions on Information Theory*, 28(2):129–137. Originally published as Bell Labs Technical Memorandum, 1957.
- Joel Max. 1960. Quantizing for minimum distortion. *IRE Transactions on Information Theory*, 6(1):7–12.
- Stephen Merity, Caiming Xiong, James Bradbury, and Richard Socher. 2017. Pointer sentinel mixture models. In *International Conference on Learning Representations (ICLR)*.
- Todor Mihaylov, Peter Clark, Tushar Khot, and Ashish Sabharwal. 2018. Can a suit of armor conduct electricity? a new dataset for open book question answering. In *Empirical Methods in Natural Language Processing (EMNLP)*.
- Denis Paperno, Germ n Kruszewski, Angeliki Lazaridou, Ngoc Quan Pham, Raffaella Bernardi, Sandro Pezzelle, Marco Baroni, Gemma Boleda, and Raquel Fern andez. 2016. The LAMBADA dataset: Word prediction requiring a broad discourse context. In *Annual Meeting of the Association for Computational Linguistics (ACL)*.

- John G Proakis and Masoud Salehi. 2008. *Digital Communications*. McGraw-Hill.
- Melissa Roemmele, Cosmin Adrian Bejan, and Andrew S Gordon. 2011. Choice of plausible alternatives: An evaluation of commonsense causal reasoning. In *AAAI Spring Symposium*.
- Wenqi Shao, Mengzhao Chen, Zhaoyang Zhang, Peng Xu, Lirui Zhao, Zhiqian Li, Kaipeng Zhang, Peng Gao, Yu Qiao, and Ping Luo. 2024. OmniQuant: Omnidirectionally calibrated quantization for large language models. In *International Conference on Learning Representations (ICLR)*.
- Hugo Touvron, Louis Martin, Kevin Stone, Peter Albert, Amjad Almahairi, Yasmine Babaei, Nikolay Bashlykov, Soumya Batra, Prajwal Bhargava, Shruti Bhosale, Dan Bikel, Lukas Blecher, Cristian Canton Ferrer, Moya Chen, Guillem Cucurull, David Esiobu, Jude Fernandes, Jeremy Fu, Wenyin Fu, and 49 others. 2023. Llama 2: Open foundation and fine-tuned chat models. *arXiv preprint arXiv:2307.09288*.
- Albert Tseng, Jerry Chee, Qingyao Sun, Volodymyr Kuleshov, and Christopher De Sa. 2024a. QuIP#: Even better LLM quantization with Hadamard incoherence and lattice codebooks. In *Proceedings of the 41st International Conference on Machine Learning (ICML)*.
- Albert Tseng, Qingyao Sun, David Hou, and Christopher De Sa. 2024b. QTIP: Quantization with trellises and incoherence processing. In *Advances in Neural Information Processing Systems (NeurIPS)*. Spotlight.
- Mart van Baalen, Andrey Kuzmin, Markus Nagel, Peter Couperus, Cedric Bastoul, Eric Mahurin, Tijmen Blankevoort, and Paul Whatmough. 2024. GPTVQ: The blessing of dimensionality for LLM quantization. In *ICML Workshop on Efficient Systems for Foundation Models (ES-FoMo)*.
- Caio Vicentino. 2026. PolarQuant: Optimal Gaussian weight quantization via Hadamard rotation for LLM compression. *arXiv preprint arXiv:2603.29078* (withdrawn; later rebranded as HLWQ).
- Alex Wang, Amanpreet Singh, Julian Michael, Felix Hill, Omer Levy, and Samuel R Bowman. 2018. GLUE: A multi-task benchmark and analysis platform for natural language understanding. In *EMNLP BlackboxNLP Workshop*. RTE recognized as part of the GLUE benchmark.
- Guangxuan Xiao, Ji Lin, Mickael Seznec, Hao Wu, Julien Demouth, and Song Han. 2023. Smoothquant: Accurate and efficient post-training quantization for large language models. In *Proceedings of the 40th International Conference on Machine Learning (ICML)*.
- An Yang, Baosong Yang, Beichen Zhang, Binyuan Hui, Bo Zheng, Bowen Yu, Chengyuan Li, Dayiheng Liu, Fei Huang, Haoran Wei, and 1 others. 2024. Qwen2.5 technical report. *arXiv preprint arXiv:2412.15115*.
- Paul L Zador. 1982. Asymptotic quantization error of continuous signals and the quantization dimension. *IEEE Transactions on Information Theory*, 28(2):139–149.
- Rowan Zellers, Ari Holtzman, Yonatan Bisk, Ali Farhadi, and Yejin Choi. 2019. HellaSwag: Can a machine really finish your sentence? In *Annual Meeting of the Association for Computational Linguistics (ACL)*.
- Peiyuan Zhang, Guangtao Zeng, Tianduo Wang, and Wei Lu. 2024. TinyLlama: An open-source small language model. *arXiv preprint arXiv:2401.02385*.

## A Codec-Level Analysis

With the encoder/decoder fixed (section 3), the two codec operations that determine directional reconstruction error are the block-Hadamard rotation and the per-pair quantizer. Each is analyzed in turn: the rotation as an exact isometry, and the polar amplitude-phase decomposition as the baseline against which the joint 2D codebook is judged. Layer-output effects — how this directional error translates to perturbations under real activations — are deferred to section B.

### A.1 Analysis I: Rotation Isometry

The normalized row is transformed by a sign-masked block-Hadamard rotation. This rotation is an exact isometry in real arithmetic, so it cannot add mathematical distortion by itself. Its practical role is to reduce coordinate coherence and spread energy within each block before quantization; the circular-Gaussian model used by the pair codebooks is calibrated empirically and does not follow from orthogonality alone.

**Definition A.1** (Unnormalized Walsh-Hadamard matrix). For any integer  $b = 2^m$  with  $m \geq 0$ , the unnormalized Walsh-Hadamard matrix  $H_b \in \{-1, +1\}^{b \times b}$  is defined recursively by  $H_1 = [1]$  and

$$H_{2b} = \begin{bmatrix} H_b & H_b \\ H_b & -H_b \end{bmatrix}. \quad (4)$$

It satisfies  $H_b^\top H_b = bI$  and  $H_b = H_b^\top$ .

**Definition A.2** (Block-normalized Hadamard transform). Let  $b$  be a power of two dividing  $d_{\text{in}}$ . The normalized block-Hadamard matrix  $F \in \mathbb{R}^{d_{\text{in}} \times d_{\text{in}}}$  is block diagonal with  $d_{\text{in}}/b$  identical blocks, each equal to  $(1/\sqrt{b})H_b$ :

$$F = \frac{1}{\sqrt{b}} \underbrace{H_b \oplus \cdots \oplus H_b}_{d/b \text{ blocks}}. \quad (5)$$

**Definition A.3** (Sign mask). Let  $s_1, \dots, s_{d_{\text{in}}} \in \{\pm 1\}$  be a deterministic sequence generated from a fixed 64-bit seed. The sign mask is the diagonal matrix  $S = \text{diag}(s_1, \dots, s_{d_{\text{in}}})$ .

**Lemma 1** (Block-Hadamard rotation isometry). Assume  $d_{\text{in}} = mb$  for integers  $m \geq 1$  and  $b = 2^q$  with  $q \geq 1$ . Let  $F = I_m \otimes b^{-1/2}H_b$  be the block-normalized Hadamard matrix and  $S = \text{diag}(s_1, \dots, s_{d_{\text{in}}})$  with  $s_j \in \{\pm 1\}$ . With  $R_{\text{fwd}} = FS$  and  $R_{\text{inv}} = SF$ , both maps are orthogonal in exact real arithmetic ( $R_{\text{fwd}}^\top R_{\text{fwd}} = R_{\text{inv}}^\top R_{\text{inv}} = I$ ), mutually inverse ( $R_{\text{inv}} R_{\text{fwd}} = I$ ), and preserve norms, distances, inner products, and per-block energy.

*Proof.*  $H_b^\top H_b = bI$  and  $H_b = H_b^\top$ , so each normalized block  $b^{-1/2}H_b$  is orthogonal and symmetric.  $F$  is block diagonal with these blocks, giving  $F^\top F = I$  and  $F^\top = F$ .  $S$  is diagonal with  $\pm 1$  entries, so  $S^\top = S$  and  $S^2 = I$ . Then  $R_{\text{fwd}}^\top R_{\text{fwd}} = SF^\top FS = I$  and  $R_{\text{inv}} R_{\text{fwd}} = SF \cdot FS = SF^2S = I$ . Norm, distance, and inner-product preservation follow from orthogonality; per-block energy preservation follows because  $F$  and  $S$  act independently within each block of the partition.  $\square$

*Remark A.1.* The lemma is purely geometric. It proves that the rotation contributes no mathematical distortion and that quantization error has the same Euclidean norm before and after the inverse rotation. It does not prove that the rotated coordinates are independent or Gaussian. If the signs are idealized as independent Rademacher variables, then for a fixed vector  $v$  and coordinate  $j$  in block  $B(j)$ ,

$$\begin{aligned} \mathbb{E}_S[(R_{\text{fwd}}v)_j] &= 0, \\ \mathbb{E}_S[(R_{\text{fwd}}v)_j^2] &= \frac{\|v_{B(j)}\|_2^2}{b}. \end{aligned}$$

This explains the energy-spreading intuition within each block. Approximate Gaussianity requires the usual incoherence condition that no small number of input coordinates dominates the signed sum, and is checked empirically through calibration.

*Remark A.2.* The forward and inverse matrices are generally different because  $F$  and  $S$  do not commute. The sign-masked transform is orthogonal, but it is not generally symmetric and is not generally an involution.

## A.2 Analysis II: Polar Pair Distortion

The second codec-level theorem analyzes the polar baseline from section 3. The theorem gives a deterministic amplitude-phase decomposition; the following corollary adds the Rayleigh/Lloyd source model used to compare independent amplitude-phase coding against joint 2D QAM.

**Theorem 1** (Polar QAM pair distortion decomposition). For a complex pair  $z = ae^{i\theta}$  and reconstruction  $\hat{z} = \hat{a}e^{i\hat{\theta}}$ ,

$$\|z - \hat{z}\|^2 = (a - \hat{a})^2 + 2a\hat{a}(1 - \cos(\theta - \hat{\theta})). \quad (6)$$

If  $a, \hat{a}, \theta, \hat{\theta}$  are random variables with finite second moments and  $\delta = \text{wrap}(\theta - \hat{\theta})$ , then

$$\mathbb{E}\|z - \hat{z}\|^2 = \mathbb{E}(a - \hat{a})^2 + 2\mathbb{E}[a\hat{a}(1 - \cos \delta)]. \quad (7)$$

*Proof.* The deterministic identity follows by expanding

$$\begin{aligned} |ae^{i\theta} - \hat{a}e^{i\hat{\theta}}|^2 &= a^2 + \hat{a}^2 - 2a\hat{a}\cos(\theta - \hat{\theta}) \\ &= (a - \hat{a})^2 \\ &\quad + 2a\hat{a}(1 - \cos(\theta - \hat{\theta})). \end{aligned}$$

Because cosine is  $2\pi$ -periodic, replacing  $\theta - \hat{\theta}$  by the wrapped error  $\delta$  does not change the expression. Taking expectations gives the second claim.  $\square$

**Corollary 1** (Rayleigh-Lloyd polar distortion bound). Assume the circular-Gaussian model for pair  $k$ :  $a = \sigma_k U$  with  $U \sim \text{Rayleigh}(1)$ ,  $\theta$  is uniform on  $(-\pi, \pi]$ , and  $a$  and  $\theta$  are independent. Let  $Q_a$  be an  $N_a$ -level Lloyd-Max quantizer for  $U$  under squared error, with normalized distortion  $C_{\text{LM}}(N_a) = \mathbb{E}(U - Q_a(U))^2$ , and set  $\hat{a} = \sigma_k Q_a(U)$ . Let the phase quantizer round  $\theta$  to the nearest one of  $N_p$  uniform phase levels, with bin centers aligned to the grid  $\{(2k+1)h : k = 0, 1, \dots, N_p-1\}$  modulo  $2\pi$ , where  $h = \pi/N_p$  (so that adjacent phase bin boundaries are spaced by  $2h$  and bin centers sit at midpoints). Then

$$\begin{aligned} \mathbb{E}\|z - \hat{z}\|^2 &= \sigma_k^2 C_{\text{LM}}(N_a) \\ &\quad + 2\sigma_k^2 M_a(N_a)\eta(N_p), \end{aligned} \quad (8)$$

where

$$\begin{aligned} M_a(N_a) &= \mathbb{E}[U Q_a(U)], \\ \eta(N_p) &= 1 - \frac{\sin(\pi/N_p)}{\pi/N_p}. \end{aligned} \quad (9)$$

For a centroid Lloyd-Max quantizer,  $M_a(N_a) = 2 - C_{\text{LM}}(N_a)$ , hence

$$\mathbb{E}\|z - \hat{z}\|^2 = \sigma_k^2 \left[ C_{\text{LM}}(N_a) + 2(2 - C_{\text{LM}}(N_a))\eta(N_p) \right] \quad (10)$$

and

$$\mathbb{E}\|z - \hat{z}\|^2 \leq \sigma_k^2 \left[ C_{\text{LM}}(N_a) + (2 - C_{\text{LM}}(N_a)) \frac{\pi^2}{3N_p^2} \right]. \quad (11)$$

*Proof.* The amplitude contribution is  $\mathbb{E}(a - \hat{a})^2 = \sigma_k^2 C_{\text{LM}}(N_a)$  by the definition of the normalized Lloyd-Max distortion. Under the circular-Gaussian model, amplitude and phase are independent. Because  $\theta$  is uniform on  $(-\pi, \pi]$  and the phase quantizer is uniform with bin centers aligned to multiples of  $2h$  (the hypothesis on the phase grid), nearest-level rounding produces a wrapped phase error  $\delta$  that is uniform on  $[-h, h]$  with  $h = \pi/N_p$ , independent of  $a$  and  $\hat{a}$ . Hence

$$\begin{aligned} \mathbb{E}(1 - \cos \delta) &= 1 - \frac{1}{2h} \int_{-h}^h \cos t \, dt \\ &= 1 - \frac{\sin h}{h} = \eta(N_p). \end{aligned} \quad (12)$$

The phase contribution is therefore  $2\mathbb{E}[a\hat{a}]\eta(N_p) = 2\sigma_k^2 M_a(N_a)\eta(N_p)$ .

For a centroid Lloyd-Max quantizer,  $Q_a(U) = \mathbb{E}[U | Q_a(U)]$  on each cell. By the tower property and the centroid identity, and noting that  $Q_a(U)$  is  $\sigma(Q_a(U))$ -measurable so it pulls inside the conditional expectation,

$$\begin{aligned} M_a(N_a) &= \mathbb{E}[UQ_a(U)] \\ &= \mathbb{E}[\mathbb{E}[U | Q_a(U)] \cdot Q_a(U)] \\ &= \mathbb{E}[Q_a(U)^2]. \end{aligned} \quad (13)$$

Since  $\mathbb{E}U^2 = 2$  for the unit Rayleigh law,

$$\begin{aligned} C_{\text{LM}}(N_a) &= \mathbb{E}(U - Q_a(U))^2 \\ &= \mathbb{E}U^2 - \mathbb{E}[Q_a(U)^2] = 2 - M_a(N_a), \end{aligned} \quad (14)$$

which gives  $M_a(N_a) = 2 - C_{\text{LM}}(N_a)$ . Finally, the bound  $1 - \sin h/h \leq h^2/6$  follows from the Taylor expansion  $\sin h = h - h^3/6 + O(h^5)$ , valid for  $h \in [0, \pi]$  (the remainder is non-negative on this interval since the next term is  $+h^5/120$  and the series is alternating with decreasing magnitude). Substituting  $h = \pi/N_p$  gives  $2(2 - C_{\text{LM}}(N_a))\eta(N_p) \leq (2 - C_{\text{LM}}(N_a))\pi^2/(3N_p^2)$ .  $\square$

*Remark A.3.* The bound is an idealized source-model statement. The implementation uses a finite Rayleigh integration cutoff  $R_{\text{max}} = 8$  and f32 codebook levels, so its  $C_{\text{LM}}$  is the numerically integrated distortion of that practical codebook. The Rayleigh tail beyond  $8\sigma_k$  is negligible for the reported bit budgets, but the exact equality above should be read as the population calculation for the ideal Rayleigh source and nearest uniform phase quantizer.

### A.3 Rotated-Domain Error Accounting

Each complex pair contains two scalar coordinates. Because the inverse rotation is an isometry, the squared error of the unnormalized inverse-rotated direction is the sum of pairwise errors:

$$\begin{aligned} \|u - \tilde{u}\|_2^2 &= \|R_{\text{fwd}}u - \hat{y}\|_2^2 = \sum_k \|z_k - \hat{z}_k\|^2, \\ \tilde{u} &= R_{\text{inv}}\hat{y}. \end{aligned} \quad (15)$$

If the decoder subsequently normalizes  $\tilde{u}$  before multiplying by the stored row norm, that final radial projection is a separate step; the equality above applies to the linear inverse-rotation stage.

**Corollary 2** (Direction and per-coordinate reporting). *Let each pair error be  $e_k = \|z_k - \hat{z}_k\|^2$ . Before the optional final direction renormalization,*

$$\begin{aligned} \|u - \tilde{u}\|_2^2 &= \sum_k e_k, \\ \text{MSE}_{\text{coord}} &= \frac{1}{d} \sum_k e_k = \frac{1}{2} \text{mean}_k(e_k). \end{aligned} \quad (16)$$

*If  $u$  and  $\hat{u}$  are both unit vectors, then the cosine loss is exactly*

$$1 - \langle u, \hat{u} \rangle = \frac{1}{2} \|u - \hat{u}\|_2^2. \quad (17)$$

*Proof.* The first identity is the rotated-domain error equality above, and the per-coordinate statement only divides by the  $d = 2 \#\{k\}$  scalar coordinates. For unit vectors,  $\|u - \hat{u}\|_2^2 = \|u\|_2^2 + \|\hat{u}\|_2^2 - 2\langle u, \hat{u} \rangle = 2(1 - \langle u, \hat{u} \rangle)$ .  $\square$

### A.4 Empirical Check of the Circular-Gaussian Model

Corollary 1 and the Lloyd codebook training in section 3.4 both invoke the circular-Gaussian model for the post-rotation pair distribution. Whether this model is a useful idealization of empirical transformer weights is a separable question that can

be checked directly. For each of the three target architectures, one representative MLP down\_proj matrix is processed with the same pipeline used by the codec: a sign-masked block-Hadamard rotation at  $b = 1024$  block size, per-row unit normalization, and sampling of 50,000 rotated complex pairs. The marginal distributions of the magnitude  $|z|$  are then compared to a fitted Rayleigh law, and of the real part  $\Re(z)$  to a fitted zero-mean Gaussian, via QQ plots (fig. 3).

Figure 3 shows the empirical check: one representative mlp.down\_proj matrix per architecture, 50,000 rotated complex pairs after the same sign-masked block-Hadamard rotation the codec uses. The body of the distribution tracks the Rayleigh (magnitude) and zero-mean Gaussian (real-part) marginals closely; departures appear only in the far tail, which the Lloyd training implicitly down-weights through the density-weighted MSE objective. The post-rotation distribution is therefore close enough to the circular-Gaussian model that the analytical results based on it are an informative guide to codec behaviour, not a placeholder assumption.

## B Layer Output Error and Activation Awareness

section A established that the codec’s reconstruction error is directional and controlled, to first order, by the per-pair Lloyd distortion. Quality at the model level, however, is not measured in weight space directly: a quantized layer is judged by how its output deviates from the BF16 output under the activations it actually sees. This section bridges weight error to layer-output error via a closed-form trace identity, then uses that identity to motivate AWQ-style per-channel scaling.

**Notation.** Throughout this and the following sections,  $\hat{M}_x = X^\top X$  is the unnormalized activation second-moment matrix ( $X \in \mathbb{R}^{n \times d_{\text{in}}}$ , with  $n$  activation rows in the calibration batch), and  $M_x = \hat{M}_x/n$  is its per-token-normalized form. Both forms appear;  $\hat{M}_x$  in finite-sample empirical identities and  $M_x$  when stating per-sample expectations or when referring to a random activation row’s second moment.

### B.1 Activation-Weighted Layer Error

**Proposition B.1** (Layer output error identity). *Let  $W, \hat{W} \in \mathbb{R}^{d_{\text{out}} \times d_{\text{in}}}$  with  $\Delta W = W - \hat{W}$ , and let  $X \in \mathbb{R}^{n \times d_{\text{in}}}$  be a row-major matrix of layer-*

*input activation vectors with  $n \geq 1$ . The identity conditions on the same input activations  $X$  being supplied to the original and quantized layer; if earlier quantized layers perturb  $X$ , that propagation effect is outside this single-layer statement. Define the unnormalized activation second-moment matrix  $\hat{M}_x = X^\top X$ . Then*

$$\begin{aligned} \|XW^\top - X\hat{W}^\top\|_F^2 &= \|X\Delta W^\top\|_F^2 \\ &= \text{Tr}(\Delta W \hat{M}_x \Delta W^\top). \end{aligned} \quad (18)$$

*With  $M_x = \frac{1}{n}X^\top X$ , the mean per-sample squared output error is*

$$\frac{1}{n} \|X\Delta W^\top\|_F^2 = \text{Tr}(\Delta W M_x \Delta W^\top). \quad (19)$$

*Equivalently, for a random activation row  $x \in \mathbb{R}^{d_{\text{in}}}$  with finite second moment  $M_x = \mathbb{E}[x^\top x]$ ,*

$$\mathbb{E} \left[ \|xW^\top - x\hat{W}^\top\|_2^2 \right] = \text{Tr}(\Delta W M_x \Delta W^\top). \quad (20)$$

*Proof.*

$$\begin{aligned} \|X\Delta W^\top\|_F^2 &= \text{Tr} \left[ (X\Delta W^\top)(X\Delta W^\top)^\top \right] \\ &= \text{Tr}(X\Delta W^\top \Delta W X^\top) \\ &= \text{Tr}(\Delta W X^\top X \Delta W^\top). \end{aligned}$$

Dividing by  $n$  gives the empirical mean. The random-activation statement is the same identity with  $M_x = \mathbb{E}[x^\top x]$ .  $\square$

This identity shows that the relevant layer objective is not unweighted weight MSE,  $\|\Delta W\|_F^2$ , but activation-weighted error on the calibration activations. Unweighted MSE is recovered only when  $M_x$  is proportional to the identity. The matrix  $M_x$  is an uncentered second moment; it equals the covariance only when activations have zero mean. The implementation reports the relative layer-output RMSE

$$\frac{\|XW^\top - X\hat{W}^\top\|_F}{\|XW^\top\|_F}, \quad (21)$$

which is the proposition’s numerator normalized by the BF16 layer-output norm.

**Corollary 3** (Diagonal activation-RMS surrogate). *If the normalized activation second moment is diagonal,  $M_x = \text{diag}(r_1^2, \dots, r_{d_{\text{in}}}^2)$ , then*

$$\frac{1}{n} \|X\Delta W^\top\|_F^2 = \sum_{i=1}^{d_{\text{out}}} \sum_{j=1}^{d_{\text{in}}} r_j^2 (\Delta W_{ij})^2. \quad (22)$$

QQ check for rotated complex pairs — top: magnitude vs Rayleigh; bottom: real part vs Normal

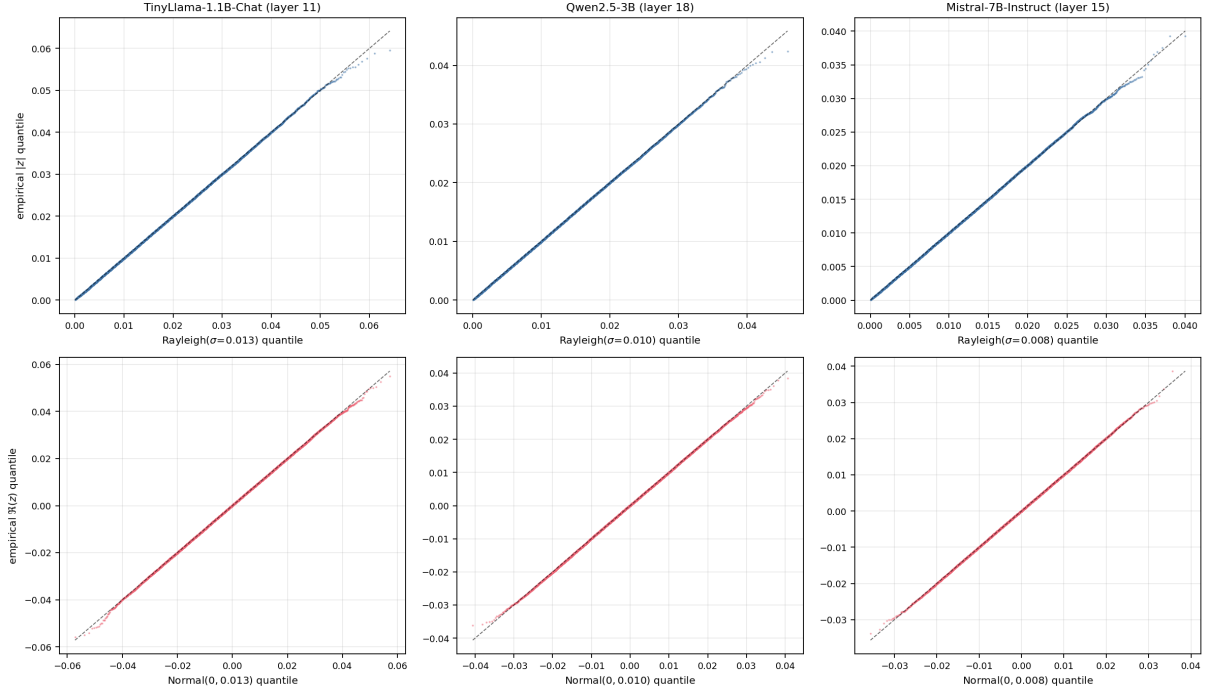


Figure 3: QQ plots for the rotated complex-pair marginals of a representative mlp. down\_proj matrix on each of the three target architectures. Top row, per architecture: empirical  $|z|$  quantiles against a Rayleigh law fitted on the same sample. Bottom row: empirical  $\Re(z)$  quantiles against a zero-mean Gaussian fitted on the same sample. Sample size per panel is 50,000 rotated pairs collected from one representative MLP down\_proj after a sign-masked block-Hadamard rotation at the same  $b=1024$  block size used by the codec. The traces lie on the  $y=x$  identity through the body of the distribution and depart only in the far tail. The circular-Gaussian model used by corollary 1 is therefore a reasonable working idealization in the regime that dominates the Lloyd objective.

For empirical calibration activations,  $r_j^2 = n^{-1} \sum_{t=1}^n X_{tj}^2$  is the squared RMS of input channel  $j$ .

*Proof.* Substitute the diagonal  $M_x$  into proposition B.1:

$$\begin{aligned} \text{Tr}(\Delta W M_x \Delta W^\top) &= \sum_i (\Delta W M_x \Delta W^\top)_{ii} \\ &= \sum_{i,j} r_j^2 (\Delta W_{ij})^2. \end{aligned}$$

The empirical formula for  $r_j^2$  is the  $j$ th diagonal entry of  $n^{-1} X^\top X$ .  $\square$

When  $M_x$  is not diagonal, this expression is a diagonal approximation that ignores cross-channel activation correlations in the current input basis. It still gives the operative AWQ-style intuition: errors in high-RMS channels matter more to the layer output than equal-sized errors in low-RMS channels.

## B.2 Activation-Aware Scaling

QAM-W uses AWQ-inspired per-input-channel scaling before quantization. For scaling factors

$s_j > 0$  and  $D_s = \text{diag}(s_1, \dots, s_{d_{\text{in}}})$ ,

$$W_{\text{scaled}} = W D_s, \quad (23)$$

$$\hat{W}_{\text{scaled}} = \text{Quantize}(W_{\text{scaled}}), \quad (24)$$

$$\hat{W} = \hat{W}_{\text{scaled}} D_s^{-1}. \quad (25)$$

The implementation sets  $s_j \propto r_j^\alpha$  with  $\alpha \in \{0.3, 0.5, 0.8\}$ , normalizes the geometric mean of the scales to one, and clamps scales to  $[1/16, 16]$ .

**Proposition B.2** (Sufficient-condition model for activation-aware scaling). *Let  $E_s = W_{\text{scaled}} - \hat{W}_{\text{scaled}}$  be the quantization error in the scaled domain, with expectation taken over the quantizer randomness alone for a fixed (deterministic) weight matrix  $W$ . Assume:*

- (A1) Scale-invariant distortion: *the per-coordinate quantization error satisfies  $\mathbb{E}[(E_s)_{ij}^2] \leq c_{ij}$  for bounded constants  $c_{ij}$  that do not depend on the scaling factors  $s_1, \dots, s_{d_{\text{in}}}$ .*
- (A2) Diagonal activation second moment:  *$M_x = \text{diag}(r_1^2, \dots, r_{d_{\text{in}}}^2)$ , as in corollary 3.*

(A3) Unclamped power-law scaling:  $s_j \propto r_j^\alpha$  for some  $\alpha \in [0, 1]$ , with the global geometric-mean normalization absorbed into  $W$  and no per-channel clipping.

Then the de-scaled error  $\Delta W^{(s)} = W - \hat{W} = E_s D_s^{-1}$  satisfies  $\mathbb{E}[(\Delta W_{ij}^{(s)})^2] = \mathbb{E}[(E_s)_{ij}^2]/s_j^2 \leq c_{ij}/s_j^2$ , where the equality uses  $\Delta W_{ij}^{(s)} = (E_s)_{ij}/s_j$  with  $s_j$  deterministic and the inequality is (A1). Under (A2) and corollary 3, the activation-weighted error satisfies

$$\mathcal{E}_{\text{act}}(s) = \sum_{i,j} r_j^2 \mathbb{E}[(\Delta W_{ij}^{(s)})^2] \leq \sum_{i,j} c_{ij} \frac{r_j^2}{s_j^2}. \quad (26)$$

Under (A3) the channel factor changes from  $r_j^2$  to  $r_j^{2(1-\alpha)}$ , attenuating the activation-weighted contribution of high-RMS channels.

*Proof.* With  $W$  fixed and the expectation taken over the quantizer randomness only,  $\Delta W_{ij}^{(s)} = (E_s)_{ij}/s_j$  with  $s_j$  deterministic, so  $\mathbb{E}[(\Delta W_{ij}^{(s)})^2] = \mathbb{E}[(E_s)_{ij}^2]/s_j^2$ . Assumption (A1)—independence of  $c_{ij}$  from  $s$ —is what makes this division valid as a uniform bound across the choice of scales:  $\mathbb{E}[(\Delta W_{ij}^{(s)})^2] \leq c_{ij}/s_j^2$ . Substituting into the diagonal- $M_x$  identity from corollary 3 (which is (A2)) gives  $\mathcal{E}_{\text{act}}(s) = \sum_{i,j} r_j^2 \mathbb{E}[(\Delta W_{ij}^{(s)})^2] \leq \sum_{i,j} c_{ij} r_j^2/s_j^2$ . Under (A3),  $s_j \propto r_j^\alpha$  with global normalization absorbed into  $W$  and no clipping, so the channel factor  $r_j^2/s_j^2$  is proportional to  $r_j^{2(1-\alpha)}$ .  $\square$

The proposition is a design model rather than a universal guarantee; it describes how (A1)–(A3) interact, and the deployed quantizer satisfies all three only approximately. Real quantizers are non-linear: codebook boundaries, row renormalization, and non-uniform Lloyd levels all change the effective source distribution, so (A1) fails when the constants  $c_{ij}$  shift with  $s$  under aggressive scaling. Section D probes (A1) directly on a representative MLP `down_proj` layer of Mistral-7B and finds that the median  $c_j$  is essentially flat across  $\alpha \in [0, 0.8]$  but the maximum  $c_j$  grows  $\sim 50\times$ , so (A1) holds in the bulk and fails in the tail; the deployed  $\alpha = 0.3$  sits well below the failure regime. Activation-aware scaling is therefore treated as an objective-motivated variant whose behaviour is checked empirically via layer-output RMSE and paired KL rather than asserted from the design model.

### B.3 Empirical Check of the Layer-Output Identity

Proposition B.1 is exact, so it does not need empirical validation as a mathematical statement. The operational claim that follows from it — that unweighted weight Frobenius  $\|\Delta W\|_F/\|W\|_F$  is a worse proxy for what the model actually computes than the activation-weighted layer-output RMSE  $\sqrt{\text{Tr}(\Delta W M_x \Delta W^\top)/\text{Tr}(W M_x W^\top)}$  — does. Table 4 reports both quantities (averaged across the 96 MLP linear layers of Mistral-7B-Instruct-v0.3) for four methods spanning two orders of magnitude in  $\Delta\text{PPL}\%$ . The  $M_x$  matrices are computed from forward-pass activations of the BF16 reference on eight WikiText-2 sequences of length 2048.

Two observations from table 4 support the operational reading of proposition B.1.

**Method-dependent amplification.** The activation-weighting amplification factor `amp.med.` varies by nearly  $2\times$  across the four methods. GPTQ’s Hessian-aware optimization aligns its residual error with low- $M_x$  directions and earns the largest discount (median  $\rho_o/\rho_w = 0.57$ ): the activation-weighted layer-output RMSE is  $\sim 1.8\times$  smaller than the unweighted weight Frobenius would suggest. AWQ does not earn the same discount (median 0.95): its weight error is roughly isotropic with respect to  $M_x$ , so the activation weighting barely changes the apparent magnitude. SmoothQuant and the activation-aware joint-2D codec sit in between (0.87 and 0.83 respectively). At equal raw weight Frobenius, two methods can therefore differ substantially on what the model actually computes; weight Frobenius alone is not enough to rank them.

**Per-layer spread.** The amplification factor also has substantial *within*-method spread. For AWQ the per-layer ratio ranges from 0.55 to 5.53 across the 96 layers (std. 0.50); the maximum corresponds to the embedding-adjacent MLP block where the AWQ error happens to project disproportionately onto high- $M_x$  directions, and the model output inherits the full hit. GPTQ’s per-layer ratio, by contrast, sits in a tight  $[0.24, 0.69]$  band (std. 0.12). This is direct evidence that the layer-output identity is doing real work: two layers with the same  $\|\Delta W\|_F$  can produce layer-output error that differs by an order of magnitude depending on how that error aligns with the calibration  $M_x$ . The codec

Table 4: Empirical anchor for proposition B.1: per-layer unweighted weight Frobenius and activation-weighted layer-output RMSE, averaged over the 96 MLP linear layers of Mistral 7B (checkpoints from the MLP + attention quantization extension, section F.1). The *amp.* column is the median per-layer ratio  $\rho_o/\rho_w$ , where  $\rho_w = \|\Delta W\|_F/\|W\|_F$  and  $\rho_o^2 = \text{Tr}(\Delta W M_x \Delta W^\top)/\text{Tr}(W M_x W^\top)$ . Mean KL and  $\Delta\text{PPL}\%$  are from table 6. *Reader key:*  $\downarrow$  lower is better. Shaded rows ( $\star$ ) are QAM-W (ours).

method	$\rho_w \downarrow$	$\rho_o \downarrow$	amp. med.	mean KL $\downarrow$	$\Delta\text{PPL}\% \downarrow$
SmoothQuant W8A8	0.011	0.009	0.87	0.0008	+0.04%
$\star$ QAM-W-5.5	0.033	0.025	0.83	0.0024	+0.11%
GPTQ W4A16 g128	0.135	0.070	0.57	0.0204	+1.43%
AWQ W4A16 g128	0.332	0.340	0.95	0.0310	+2.88%

that explicitly accounts for  $M_x$  via per-channel scaling — whether at calibration time (GPTQ) or at quantization time (QAM-W with  $\alpha = 0.3$ ) — earns a measurable reduction in  $\rho_o$  that unweighted Frobenius cannot see.

## C From Codec Error to Model Behavior

Proposition B.1 maps weight error to layer-output error. Section A earlier derived per-pair codec distortion. This section closes the chain to model behavior with a local logit-KL bridge, then composes the three steps into a single monotone upper bound whose codec-dependent ingredient is the per-pair Lloyd distortion  $D_B$  on the unit circular Gaussian. The bound is tested empirically in sections 5.1 and 5.3.2: if informative, measured paired KL should be rank-correlated with  $D_B$  across methods at fixed architecture.

### C.1 Logit Perturbation and Local KL Bridge

Let  $f(x)$  be the BF16 logits and  $\hat{f}(x)$  the logits under quantized weights, with  $\delta = \hat{f}(x) - f(x)$ . If the transformer computation after the perturbed linear layers is locally Lipschitz around the evaluation activation trajectories, then the logit perturbation is controlled by the accumulated layer-output perturbations,

$$\|\delta\|_2 \lesssim L \sum_{\ell} \|X_{\ell} \Delta W_{\ell}^{\top}\|_F. \quad (27)$$

The constant  $L$  is not estimated here because norm-only Lipschitz bounds for transformers are usually too loose to be useful. The structural point is that activation-weighted layer error is the quantity that propagates, not raw weight MSE.

**Corollary 4** (Local logit-KL bridge). *Let  $p = \text{softmax}(f)$  and  $q = \text{softmax}(f + \delta)$  with logit Hessian  $F_p = \text{diag}(p) - pp^{\top}$ . Then*

$$D_{\text{KL}}(p\|q) = \frac{1}{2} \delta^{\top} F_p \delta + r(\delta), \quad (28)$$

where the third-order Lagrange remainder satisfies  $|r(\delta)| \leq \frac{1}{3} \|\delta\|_2^3$  (proof below; the softmax cumulant tensor’s operator-3-norm on the unit sphere is bounded by  $\sqrt{2}/2 \leq 1$ ). Since  $\|F_p\|_2 \leq 1/2$ , the local approximation  $D_{\text{KL}}(p\|q) \approx \frac{1}{4} \|\delta\|_2^2$  holds with absolute error  $\leq \frac{1}{3} \|\delta\|_2^3$ . Combining with (27) gives

$$D_{\text{KL}}(p\|q) \lesssim \frac{L^2}{4} \left( \sum_{\ell} \|X_{\ell} \Delta W_{\ell}^{\top}\|_F \right)^2, \quad (29)$$

valid in the regime where the cubic remainder is small relative to the quadratic term.

*Proof.* Taylor expansion of softmax cross-entropy around logits  $f$ . The first-order term vanishes because KL is minimized at  $q = p$ , and the Hessian is  $F_p$ . The operator-norm bound  $\|F_p\|_2 \leq 1/2$  follows from Popoviciu’s inequality applied to a unit-vector random variable under  $p$ . For the cubic remainder, the third-cumulant tensor of the softmax log-partition is  $T_{ijk} = \kappa_3(p)_{ijk}$ . For a unit vector  $v$  and  $I \sim p$ ,  $T(v, v, v) = \mathbb{E}_p[(v_I - \mathbb{E}_p v_I)^3]$ . Since  $\|v\|_2 = 1$  we have  $\max v - \min v \leq \sqrt{2}$ ; combining  $|\mathbb{E}[(Y - \mathbb{E}Y)^3]| \leq (\max - \min) \cdot \text{Var}(Y)$  with Popoviciu’s variance bound  $\text{Var}(Y) \leq (\max - \min)^2/4$  gives  $|T(v, v, v)| \leq (\sqrt{2})^3/4 = \sqrt{2}/2 \leq 1$ . The Lagrange remainder is  $r(\delta) = \frac{1}{6} T(\xi)(\delta, \delta, \delta)$  for some  $\xi$  on the segment, so  $|r(\delta)| \leq \frac{1}{6} \|\delta\|_2^3 < \frac{1}{3} \|\delta\|_2^3$ . Substituting (27) into the quadratic term gives the final display.  $\square$

*Remark C.1.* Realized KL can be much smaller than this bound because quantization noise is not necessarily aligned with the leading directions of  $F_p$ . We do not attempt to bound perplexity directly: it depends on the evaluation distribution, token entropy, calibration, and nonlinear error propagation, and any direct bound from  $\|\Delta W\|$  would be too loose to guide codec design. The diagnostic chain

(theorem 1  $\rightarrow$  proposition B.1  $\rightarrow$  corollary 4) maps codec to KL; perplexity is reported as the end-to-end metric.

## C.2 Composite Bound

Let  $D_B$  denote the per-pair Lloyd-Max MSE of the  $2^B$ -point planar codebook on the unit circular Gaussian (theorem 1). For a single weight row  $w \in \mathbb{R}^{d_{\text{in}}}$  with paired coordinates  $\{z_k\}$ , each pair has calibrated scale  $\sigma_k$  (section 3.4). Codebook lookup is performed on each pair after rescaling toward the codebook's source domain.

**Assumption C.1** (Linear codec response). *For pair  $k$  with per-coordinate calibration variance  $\sigma_k^2$  from section 3.4 (so  $\mathbb{E} \|z_k\|^2 = 2\sigma_k^2$  under the circular-Gaussian model), the per-pair squared reconstruction error scales with  $\sigma_k^2$ :  $\mathbb{E} \|\Delta z_k\|^2 \leq \sigma_k^2 D_B$ , where  $D_B$  is the per-pair Lloyd-Max MSE on the unit circular Gaussian (per-coordinate variance 1) and the expectation is over the quantizer applied to a row drawn from the calibration sample.*

This is exact for high-rate Lloyd codebooks applied to scaled copies of a fixed source (Lloyd, 1982; Max, 1960; Gersho and Gray, 1991; Zador, 1982). For empirical post-rotation pairs the assumption is an idealization; the QQ check (fig. 3) supports its accuracy in the bulk and fig. 4 probes its failure modes in the tail.

Summing Assumption C.1 over pairs of a single row and using Parseval (the block-Hadamard rotation is an isometry, so  $\sum_k \|z_k\|^2 = \|w\|^2$  deterministically; in expectation  $\sum_k 2\sigma_k^2 = \mathbb{E} \|w\|^2$ , hence  $\sum_k \sigma_k^2 = \frac{1}{2} \mathbb{E} \|w\|^2$ ) gives

$$\mathbb{E} \|\Delta W\|_F^2 \leq \frac{1}{2} D_B \mathbb{E} \|W\|_F^2, \quad (30)$$

where the expectation on both sides is over the calibration sample and the quantizer. Plugging (30) into the activation-weighted trace identity (proposition B.1, random-activation form,  $M_x := \mathbb{E}[x^\top x]$ ) and applying the PSD quadratic-form bound  $\text{Tr}(A M A^\top) \leq \lambda_{\max}(M) \|A\|_F^2$ ,

$$\rho_\ell^2 := \mathbb{E}_x \left[ \|x \Delta W_\ell^\top\|_2^2 \right] \leq \frac{1}{2} D_B \lambda_{\max}^{(\ell)} \|W_\ell\|_F^2, \quad (31)$$

where  $\lambda_{\max}^{(\ell)} := \lambda_{\max}(M_x^{(\ell)})$  and  $\rho_\ell$  is the per-token layer-output RMS at quantized layer  $\ell$ . Summing over the  $L_q$  quantized layers and applying Cauchy–

Schwarz,

$$\sum_{\ell=1}^{L_q} \rho_\ell \leq \sqrt{\frac{1}{2} D_B L_q C_W}, \quad (32)$$

$$C_W := \sum_{\ell=1}^{L_q} \lambda_{\max}^{(\ell)} \|W_\ell\|_F^2.$$

Composing with corollary 4 gives the composite bound below.

**Theorem 2** (Composite codec-to-KL upper bound is monotone in  $D_B$  and  $C_W$ ). *Under the assumptions of proposition B.1 and corollary 4, the upper bound on the realized paired KL divergence between the BF16 and quantized models obtained by chaining (31), (32), and corollary 4 is non-decreasing in two scalars:  $D_B$  (the per-pair Lloyd distortion of the codebook on the unit circular Gaussian) at fixed architecture, and  $C_W$  (a model-fixed constant set by the calibration activations and weight norms) at fixed codec.*

$$\mathbb{E} D_{\text{KL}}(p \| q) \lesssim U(D_B, C_W), \quad (33)$$

$$\partial U / \partial D_B \geq 0, \quad \partial U / \partial C_W \geq 0,$$

in the local regime where the cubic Taylor remainder of corollary 4 is small relative to the quadratic term.

*Proof.* Each of (31), (32), and corollary 4 is monotone non-decreasing in its codec-dependent argument. Composition of monotone non-decreasing maps is monotone non-decreasing, which establishes the partial-derivative sign of  $U$ .  $\square$

**Remark C.2** (Realized monotonicity is empirical, not theoretical). A monotone upper bound does not prove the realized quantity is monotone in the same parameters. Whether the realized  $\mathbb{E} D_{\text{KL}}$  tracks the envelope is what section C.3 measures.

**Remark C.3** (Quantitative envelope). The same proof chain, kept under tight Cauchy–Schwarz inequalities and using the worst-case post-quantization Lipschitz constant  $L$  of the transformer along the evaluation trajectory, gives the explicit bound

$$\mathbb{E} D_{\text{KL}}(p \| q) \lesssim \frac{L^2 L_q}{8} C_W D_B. \quad (34)$$

This envelope is loose:  $L$  is not directly observable,  $C_W$  involves the per-layer activation top-eigenvalue rather than a tractable diagonal surrogate, and the Cauchy–Schwarz step at (32) discards

cross-layer alignment. The empirical block tests only the monotonicity statement; (34) is reported for completeness, not as the headline claim.

Three structural consequences of theorem 2 are testable.

- (C1) *Codec dependence is linear in  $D_B$ .* At fixed model, the upper bound on  $\mathbb{E} D_{\text{KL}}$  scales linearly in  $D_B$ . For a  $2^B$ -point 2D Lloyd codebook at high rate on the unit circular Gaussian source, Zador’s formula (Zador, 1982; Gersho and Gray, 1991) gives  $D_B \sim 2G(2)2^{-B}$  with hexagonal-lattice constant  $G(2) = 5/(36\sqrt{3}) \approx 0.0802$ , so per additional bit *per pair*,  $\ln \mathbb{E} D_{\text{KL}}$  should decrease by  $\approx \ln 2 \approx 0.69$ ; per additional bit *per weight* (two pair-bits each), the predicted decrement is  $\approx 2 \ln 2 \approx 1.39$  ( $\approx 0.60$  dex).
- (C2) *Architecture enters through  $C_W$ .* The only architecture-dependent factor in the envelope is  $C_W$ , which suggests the cross-model sensitivity gradient in table 1 should track  $C_W$ .
- (C3) *Activation-aware scaling reduces effective  $D_B$ .* AWQ-style per-channel rescaling shrinks the effective Lloyd distortion by a multiplicative factor determined by the alignment between  $M_x$  and the codec’s directional error (proposition B.2). The composite bound’s first-order dependence on  $D_B$  implies that this scaling enters the KL upper bound multiplicatively at the same order.

### C.3 Empirical Validation

The composite upper bound implies one quantitative and two qualitative properties of the envelope; this subsection tests whether the realized  $\mathbb{E} D_{\text{KL}}$  tracks them.

**(C1) Rate-distortion slope.** Reading the per-method paired KL across bpw levels (tables 9 to 11), paired KL drops from  $\sim 10^{-1}$  at 4.0 bpw (polar) to  $\sim 3 \times 10^{-3}$  at 5.5 bpw (activation-aware joint-2D) to  $\sim 10^{-3}$  at 8.1 bpw (SmoothQuant W8A8) — roughly two orders of magnitude over four bits of weight, or  $\approx 0.50$  dex per bit per weight. The upper-bound prediction is  $2 \log_{10} 2 \approx 0.60$  dex per bit. The measured slope is shallower than the asymptote, which matches the bitrates in this study (4–8 bpw) being below the high-rate regime where  $D \sim 2\sigma^2 G(2) 2^{-B}$  becomes tight.

**(C2) Architecture-fixed ranking.** For each fixed architecture, table 1 shows the same method ranking (SmoothQuant W8A8  $\succ$  QAM-W-5.5  $\succ$  calibrated W4  $\succ$  uncalibrated W4 / polar). The cross-model  $\Delta\text{PPL}$  spread, by contrast, varies by an order of magnitude (fig. 2). Theorem 2 motivates this factorization: within-model dependence is on  $D_B$  alone; between-model spread enters only through  $C_W$ .

**(C3) Activation-aware shift.** QAM-W-5.5 (5.5 bpw, with activation-aware scaling) sits at lower KL than QAM-W-4 (4.0 bpw, no scaling) in tables 9 to 11; the two methods differ both in bitrate and in scaling, so the comparison is not iso-bpw, but the gap between them is largest on Qwen 2.5 — the model with the largest  $\lambda_{\text{max}}^{(\ell)}$  values per proposition B.2.

**Joint check.** Figure 1 (main text) plots measured paired KL against measured  $\Delta\text{PPL}\%$  for every (method, model) row available in the study: 24 rows from the three instruction-tuned models, 4 from the Stage D Mistral extension (section F.1), 6 from the Llama-2-7B-base frontier comparison (section 5.2), and 3 from the Llama-2-13B-base scale extension (section F.2) — 37 rows total across six model variants spanning 1.1B–13B parameters and bitrates from 2 to 8.1 bpw. The pooled Spearman correlation is  $\rho = +0.99$ . The envelope being monotone does not prove the realized quantity is, so the observed  $\rho$  is evidence that  $\mathbb{E} D_{\text{KL}}$  tracks the envelope’s ranking on this dataset rather than a guarantee that it must.

## D Empirical Check of Proposition B.2 (Assumption A1)

proposition B.2’s assumption (A1) is that the per-coordinate squared quantization error in the *scaled* domain,  $\mathbb{E}[(E_s)_{ij}^2]$ , is bounded by a constant  $c_{ij}$  that does not depend on the per-channel scaling factors  $s_j$ . The proposition uses this to argue that activation-aware scaling shrinks the activation-weighted error from a  $r_j^2$  channel weighting to a  $r_j^{2(1-\alpha)}$  weighting. The discussion at the end of section B flags A1 as the load-bearing assumption and notes that the deployed quantizer satisfies it only approximately.

This appendix tests A1 empirically. The probe is on `model.layers.16.mlp.down_proj` of Mistral-7B-Instruct-v0.3 ( $d_{\text{in}} = 14,336$  channels), and the codec is the same QAM-W joint-2D Lloyd code-

book at  $B = 11$  used in the deployed QAM-W-5.5 configuration. For each  $\alpha \in \{0.0, 0.3, 0.5, 0.8\}$ , the per-channel scaling factor  $s_j \propto r_j^\alpha$  is computed (with the geometric-mean normalization and clamp range  $[1/16, 16]$  used at deployment), the weight matrix is scaled by  $\text{diag}(s_j)$ , quantized, and the per-channel mean-squared scaled-domain residual is measured as  $c_j(\alpha) = \mathbb{E}_i [(E_s)_{ij}^2]$ .

**Reading.** A1’s “bounded constant independent of  $s$ ” claim holds approximately for the typical channel: the median  $c_j$  varies by less than  $1.3\times$  across the full  $[0, 0.8]$  grid, well inside the natural Lloyd-rounding variance. A1 *fails* in the worst-case tail: the maximum  $c_j$  grows roughly  $50\times$  from  $\alpha = 0$  to  $\alpha = 0.8$ , because row renormalization concentrates more energy into a few high-magnitude channels as  $\alpha$  grows. The deployed  $\alpha = 0.3$  is conservative relative to this tail growth (max  $c_j$  at  $\alpha = 0.3$  is an order of magnitude smaller than at  $\alpha = 0.8$ ), and the per-channel clamp range  $[1/16, 16]$  is never reached at any  $\alpha$  in the tested grid (clamp hit rate is 0% at all four points). So the proposition’s design model remains a reasonable guide for the deployed range, with the caveat that its bound is not uniformly tight against the high-RMS tail.

**Scope.** The probe is on a single representative MLP down\_proj layer of one model. Whether the same  $50\times$  tail-growth pattern holds across layers and architectures is left as empirical follow-up.

## E Low-Bit Operating Point Details

### F MLP + Self-Attention and 13B-Scale Extensions

#### F.1 MLP + Self-Attention Quantization Extension

The cross-model study reports bpw over MLP weights only — attention projections and the LM head remain BF16. The natural follow-up: if QAM-W and the strongest baselines are extended to also quantize the four self-attention projections (q\_proj, k\_proj, v\_proj, o\_proj), does the bpw-efficiency ranking persist?

The BF16 reference and the four strongest sub-8 bpw configurations from table 11 (SmoothQuant W8A8, QAM-W-5.5, GPTQ, AWQ) are re-run on Mistral-7B-Instruct-v0.3 with stage all\_linear, quantizing both MLP and self-attention. Everything else is unchanged: identical calibration corpus (128 WikiText-2 sequences for the linear-codec

baselines; per-input-channel RMS over the same 128 sequences for QAM-W-5.5), identical PPL / KL protocol, and the same six-task harness panel. The bpw column now reports a substantially larger fraction of the total model.

**Ranking is preserved.** The method ordering from table 1 (MLP only) carries over: SmoothQuant W8A8  $\succ$  QAM-W-5.5  $\succ$  GPTQ  $\succ$  AWQ. The two low-distortion methods stay within the BF16 envelope ( $\Delta\text{PPL} \leq 0.15\%$ ) and SmoothQuant remains tied with BF16 on the harness average.

**Where the extra cost goes.** Comparing against the MLP-only Mistral row of table 11, the principal change is in the 4-bit calibrated methods: GPTQ moves from +0.9% to +1.43% ( $\sim 0.5$  pp worse from quantizing attention), and AWQ from +1.8% to +2.88% ( $\sim 1.1$  pp worse). The two low-distortion methods barely change. Attention projections are slightly more sensitive than MLP projections under per-channel scalar quantization, but the 2D joint codebook and 8-bit per-channel calibration both absorb this extra sensitivity without loss.

**Implication for bpw accounting.** The bpw column of table 6 is the more representative comparison for memory-bound deployment, since it spans the full weight pool that the inference runtime loads. QAM-W-5.5 retains its  $\approx 1.5\times$  bpw advantage over SmoothQuant when both are extended to all linear layers, and its quality gap to BF16 remains within the multi-seed noise floor (table 8).

#### F.2 Scale Extension: Llama-2-13B-base

The natural follow-up question is whether the  $\approx 5.5$  bpw envelope holds at the next scale rung. Base model is Llama-2-13B, accessed as NousResearch/Llama-2-13b-hf (sha 4b54e9fd...). Protocol is identical to the rest of this paper: MLP-only quantization, stride PPL at seq\_len = 2048, stride = 1024, 16K scored tokens; paired KL on 4K scored tokens; six-task harness at limit = 300.

**The 5.5 bpw envelope holds at 13B.** QAM-W-5.5 at 5.5 bpw lands at +0.25%  $\Delta\text{PPL}$  with mean KL 0.003 and a harness average 0.003 below BF16 — inside the  $\sim 2$  percentage-point harness noise floor at limit=300. Combining across the study, the same codec on five models from four families spans +0.4% (TinyLlama) / +0.3% (Qwen-

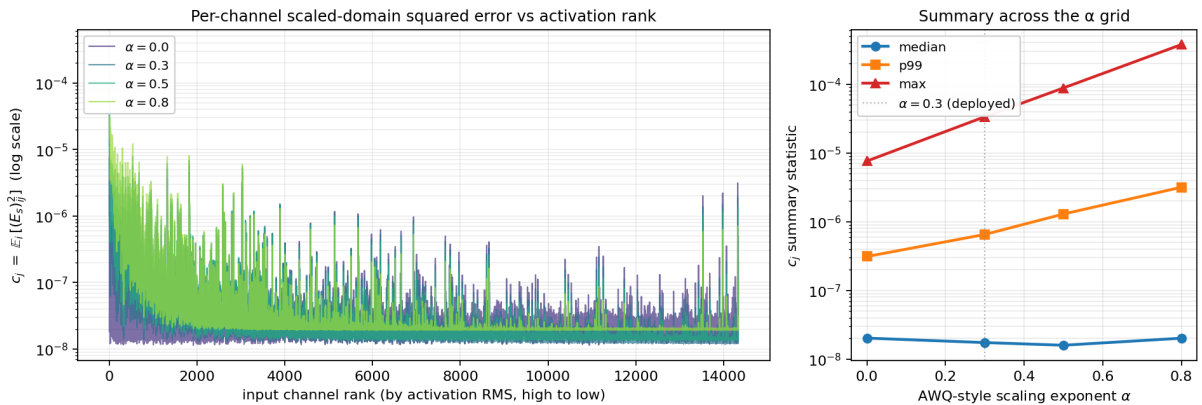


Figure 4: Empirical check of proposition B.2 (A1). Left: per-channel  $c_j$  for each  $\alpha$  in the deployed grid, channels sorted by activation RMS (highest-RMS on the left). The curves overlap closely through the bulk of the distribution and diverge at the high-activation tail. Right: median, p99, and max of  $c_j$  as a function of  $\alpha$  across all 14,336 input channels of the probed down\_proj. The median is essentially flat ( $\leq 1.3\times$  spread across the grid), p99 grows  $\sim 10\times$ , and the maximum grows  $\sim 50\times$  from  $\alpha = 0$  to  $\alpha = 0.8$ . The deployed  $\alpha = 0.3$  (dotted vertical) sits well below the regime where the worst-case channel begins to dominate.

Table 5: QAM-W-3.5 frontier. PPL is WikiText-2 stride; mean KL is paired against the BF16 reference (4K scored tokens). Bpw from each method’s manifest.

Reader key:  $\downarrow$  lower is better. Shaded rows ( $\star$ ) are QAM-W (ours).

model	config	bpw $\downarrow$	PPL $\downarrow$	$\Delta$ PPL% $\downarrow$	mean KL $\downarrow$
TinyLlama-1.1B-Chat	BF16	16.000	7.1499	—	—
TinyLlama-1.1B-Chat	$\star$ QAM-W-3.5-raw	3.506	7.6935	+7.6%	0.0724
TinyLlama-1.1B-Chat	$\star$ QAM-W-3.5	3.511	7.4396	+4.1%	0.0370
Qwen2.5-3B-Instruct	BF16	16.000	6.7826	—	—
Qwen2.5-3B-Instruct	$\star$ QAM-W-3.5-raw	3.506	7.7226	+13.9%	0.1322
Qwen2.5-3B-Instruct	$\star$ QAM-W-3.5	3.509	7.2887	+7.5%	0.0665
Mistral-7B-Instruct-v0.3	BF16	16.000	4.8883	—	—
Mistral-7B-Instruct-v0.3	$\star$ QAM-W-3.5	3.504	4.9850	+1.98%	0.0192

2.5-3B) / +0.1% (Mistral) / +0.29% (Llama-2-7B-base) / +0.25% (Llama-2-13B-base) — std 0.10 pp across the five.

### GPTQ W4A16 g128 is unusually weak at 13B.

GPTQ at 4 bpw lands at +5.05% on Llama-2-13B-base — substantially worse than on the smaller panel (TinyLlama +2.6%, Qwen +2.9%, Mistral +0.9%). This is consistent with GPTQ’s per-channel Hessian-aware optimization being sensitive to particular activation outlier patterns; the Llama-2-13B-base appears to have an unusually hostile pattern at W4A16 g128. The harness average for GPTQ (0.7363) is *higher* than BF16’s 0.7304, which is inside the harness noise floor and should be read as a tie.

**SmoothQuant is effectively lossless at 13B.** At  $\approx 8.1$  bpw SmoothQuant W8A8 (eval mode, section 5) lands at +0.02%  $\Delta$ PPL and exactly matches the BF16 harness average. QAM-W-5.5 achieves comparable quality at  $\approx 32\%$  fewer weight bits.

## G Stride-Offset Robustness of WikiText-2 Perplexity

The single-seed  $\Delta$ PPL numbers in table 1 are deterministic given the manifest’s weight hash and the corpus, but they sample only one stride-window grid over the WikiText-2 test split. To characterize the noise floor of the evaluation itself, the two principal configurations — BF16 and QAM-W-5.5 (the lowest-bpw method inside the BF16-quality envelope on this panel) — are re-

Table 6: MLP + self-attention quantization on Mistral-7B-Instruct-v0.3. *Bpw* now spans the full MLP and attention weight pool; *lm\_head* and embeddings remain BF16. Rows sorted by ascending  $\Delta$ PPL%.

Reader key:  $\downarrow$  lower is better,  $\uparrow$  higher is better. Shaded row ( $\star$ ) is QAM-W (ours).

config	bpw $\downarrow$	PPL $\downarrow$	$\Delta$ vs BF16 $\downarrow$	mean KL $\downarrow$	harness avg $\uparrow$
BF16 (ref)	16.000	4.8889	—	—	0.7597
SmoothQuant W8A8	8.128	4.8907	+0.04%	0.0008	0.7597
$\star$ QAM-W-5.5	5.506	4.8944	+0.11%	0.0024	0.7551
GPTQ W4A16 g128	4.125	4.9588	+1.43%	0.0204	0.7290
AWQ W4A16 g128	4.128	5.0299	+2.88%	0.0310	0.7404

Table 7: Llama-2-13B-base, four configurations. QAM-W-5.5 lands at +0.25%  $\Delta$ PPL, in the same envelope as table 1 and table 2.

Reader key:  $\downarrow$  lower is better,  $\uparrow$  higher is better. Shaded row ( $\star$ ) is QAM-W (ours).

config	bpw $\downarrow$	PPL $\downarrow$	$\Delta$ PPL% $\downarrow$	mean KL $\downarrow$	harness avg $\uparrow$
BF16 (ref)	16.00	4.2505	—	—	0.7304
SmoothQuant W8A8	8.13	4.2512	+0.02%	0.0007	0.7304
$\star$ QAM-W-5.5	5.50	4.2612	+0.25%	0.0029	0.7275
GPTQ W4A16 g128	4.12	4.4652	+5.05%	0.0576	0.7363

scored under three stride-window starting offsets  $\{0, 4000, 8000\}$ . Each offset shifts the window grid by a different amount and produces a near-disjoint sample of the corpus while preserving the 16K scored-token budget. Models and checkpoints are otherwise identical; *qam\_aware* is re-trained from the deployed config so the *off=0* row reproduces the single-seed table 1 value within numerical jitter.

Two readings of table 8 matter for how table 1 should be interpreted.

**Absolute PPL is noisy;  $\Delta$ PPL is not.** The absolute PPL has std 0.11–0.39 across offsets — 1–6% of the mean — because different stride-window starts land in different parts of WikiText-2 test, which have different intrinsic difficulty. But the  $\Delta$ PPL% between BF16 and QAM-W-5.5 at the *same* offset has std of only 0.03–0.08 percentage points, about an order of magnitude smaller. The codec-quality measurement factors out the corpus-position variation, which is the right behaviour for a method comparison.

**Mistral  $\Delta$ PPL is at the boundary of stride noise.** The single-seed +0.1%  $\Delta$ PPL for Mistral in table 1 sits inside the  $0.18 \pm 0.08\%$  multi-seed mean envelope: the codec degradation is real but at the same order of magnitude as the WikiText-2 stride-sampling noise floor on this model. On TinyLlama ( $+0.33 \pm 0.03\%$ ) and Qwen ( $+0.26 \pm 0.03\%$ ) the

$\Delta$ PPL is several standard deviations above zero and the relative ranking from table 1 is robust.

## H Per-Model Detail Tables

Tables tables 9 to 11 expand the headline cross-model summary in table 1 into per-architecture detail: bits-per-weight, absolute WikiText-2 perplexity,  $\Delta$ PPL% vs. BF16, paired mean KL on 4K scored tokens, and the six-task harness average. Rows are sorted by ascending  $\Delta$ PPL%; the BF16 reference row is always first. Throughout:  $\downarrow$  lower is better,  $\uparrow$  higher is better. Shaded rows ( $\star$ ) are QAM-W (ours).

## I Per-Task Harness Breakdowns

The headline cross-model harness picture is summarised by the harness-average column in tables 9 to 11 and visualised by fig. 5. For completeness, this appendix records the per-task accuracy on each of the six *lm-eval-harness* tasks (PIQA, Hel-laSwag, COPA, RTE, OpenBookQA, LAMBADA-OpenAI).

## J Reproducibility Checklist

This appendix maps the present paper against the NeurIPS reproducibility checklist and provides the exact pointers a third party would need to re-run any reported row.

Table 8: Multi-seed PPL for the two headline configurations across three stride-window starting offsets on each model. The absolute-PPL std is dominated by corpus-position variation (different offsets land in regions of WikiText-2 test with different intrinsic difficulty); the  $\Delta\text{PPL}\%$  std is an order of magnitude smaller because that corpus-position variation cancels between the two rows. The within-offset  $\Delta\text{PPL}\%$  is the right quality measure for the codec.

Reader key:  $\downarrow$  lower is better. Shaded rows ( $\star$ ) are QAM-W (ours).

model	config	PPL $\downarrow$ (mean $\pm$ std)	$\Delta\text{PPL}\%$ $\downarrow$ (mean $\pm$ std)	$n$
TinyLlama-1.1B-Chat	BF16	6.806 $\pm$ 0.391	—	3
TinyLlama-1.1B-Chat	$\star$ QAM-W-5.5	6.829 $\pm$ 0.393	+0.33 $\pm$ 0.03	3
Qwen2.5-3B-Instruct	BF16	6.653 $\pm$ 0.114	—	3
Qwen2.5-3B-Instruct	$\star$ QAM-W-5.5	6.670 $\pm$ 0.114	+0.26 $\pm$ 0.03	3
Mistral-7B-Instruct-v0.3	BF16	4.620 $\pm$ 0.262	—	3
Mistral-7B-Instruct-v0.3	$\star$ QAM-W-5.5	4.628 $\pm$ 0.259	+0.18 $\pm$ 0.08	3

Table 9: TinyLlama-1.1B-Chat. Bits-per-weight ( $bpw$ , MLP-only), WikiText-2 perplexity,  $\Delta\text{PPL}\%$  vs. BF16, paired mean KL, and six-task harness average. Bitrate range 4.006–8.129  $bpw$  + BF16 reference. Rows are sorted by descending harness average within each model. All task columns are accuracy ( $\uparrow$  higher is better); shaded rows ( $\star$ ) are QAM-W (ours).

config	$bpw$ $\downarrow$	PPL $\downarrow$	$\Delta$ vs BF16 $\downarrow$	mean KL $\downarrow$	harness avg $\uparrow$
BF16 (ref)	16.000	7.1499	—	—	0.5922
SmoothQuant W8A8	8.129	7.1586	+0.1%	0.0009	0.5985
$\star$ QAM-W-5.5	5.511	7.1752	+0.4%	0.003	0.5944
GPTQ W4A16 g128	4.125	7.3390	+2.6%	0.025	0.5914
AutoRound W4A16 g128	4.125	7.3989	+3.5%	0.033	0.5864
AWQ W4A16 g128	4.129	7.4171	+3.7%	0.038	0.5991
$\star$ QAM-W-4	4.006	7.4525	+4.2%	0.034	0.5890
RTN W4A16 g128	4.125	7.5469	+5.6%	0.055	0.6001
$\star$ QAM-W-polar	4.006	7.6246	+6.6%	0.061	0.5733

## J.1 Data and Calibration

**Evaluation corpus.** WikiText-2 raw test split, obtained via the HuggingFace datasets library; the version is pinned by the SHA-256 of the local cached \*.txt file, recorded in each eval JSON’s corpus metadata (wikitext-2-raw-v1.test.meta.json).

**Calibration corpus.** GPTQ, AWQ, AutoRound, SmoothQuant: 128 sequences of length 2048 from the WikiText-2 train split. QAM-W activation-aware variants compute per-input-channel RMS over 16 sequences of length 512 from the same WikiText-2 split, via forward-pass capture (section 5, § “Reproducibility details”). QAM-W weight-side pair-scale calibration uses up to 1024 unit-normalized rows per matrix and no activations.

**Downstream task panel.** lm-evaluation-harness at versions 0.4.11 and 0.4.12 across the study

(per-run version recorded in each eval JSON’s harness.framework\_version), no chat template, zero-shot. Batch size 16 for the cross-model main study, 8 for the Stage D extension and Llama-2-7B frontier comparison, and 4 for the Llama-2-13B scale extension (per-run value in harness.batch\_size). Six tasks (section 5.3.2); MMLU (57 subjects) added in section 5.3.2 for the two principal configurations.

## J.2 Model Provenance

The three instruction-tuned models and the two Llama-2 base models used in this paper are pinned to specific HuggingFace commit SHAs in section 5, § “Reproducibility details”. The two additional pins introduced by the Llama-2 sections:

- Llama-2-7B-base:  
NousResearch/Llama-2-7b-hf at 8efe6c9b93655b934e27bd9981e3ec13e55aee9

Table 10: Qwen2.5-3B-Instruct. Same columns as table 9; bitrate range 4.006–8.129 bpw.

config	bpw ↓	PPL ↓	$\Delta$ vs BF16 ↓	mean KL ↓	harness avg ↑
BF16 (ref)	16.000	6.7826	—	—	0.7033
SmoothQuant W8A8	8.129	6.7933	+0.2%	0.002	0.7010
★ QAM-W-5.5	5.509	6.8034	+0.3%	0.006	0.7005
GPTQ W4A16 g128	4.125	6.9781	+2.9%	0.027	0.6976
★ QAM-W-4	4.006	7.1207	+5.0%	0.062	0.6993
AutoRound W4A16 g128	4.125	7.1784	+5.8%	0.052	0.6944
AWQ W4A16 g128	4.129	7.2087	+6.3%	0.058	0.6869
★ QAM-W-polar	4.006	8.1086	+19.6%	0.187	0.6931
RTN W4A16 g128	4.125	8.4538	+24.6%	0.239	0.6673

Table 11: Mistral-7B-Instruct-v0.3. Same columns as table 9; bitrate range 4.003–8.127 bpw.

config	bpw ↓	PPL ↓	$\Delta$ vs BF16 ↓	mean KL ↓	harness avg ↑
BF16 (ref)	16.000	4.8883	—	—	0.7591
SmoothQuant W8A8	8.127	4.8894	+0.0%	0.0006	0.7591
★ QAM-W-5.5	5.505	4.8935	+0.1%	0.002	0.7534
GPTQ W4A16 g128	4.125	4.9338	+0.9%	0.014	0.7449
AutoRound W4A16 g128	4.125	4.9732	+1.7%	0.018	0.7478
AWQ W4A16 g128	4.127	4.9754	+1.8%	0.019	0.7417
RTN W4A16 g128	4.125	4.9791	+1.9%	0.021	0.7469
★ QAM-W-4	4.003	4.9824	+1.9%	0.017	0.7536
★ QAM-W-polar	4.003	5.0430	+3.2%	0.032	0.7514

d.

- Llama-2-13B-base:  
 NousResearch/Llama-2-13b-hf at 4b54e9fdd2ebd8db0901d37b98d3a53bbfaa4503.

The published QTIP and AQLM baselines (section 5.2) are pinned via their HuggingFace repo paths: relaxml/Llama-2-7b-QTIP-4Bit (03aad3088415e5ec98b1e35924719b11e29c7e45), relaxml/Llama-2-7b-QTIP-2Bit, and ISTA-DASLab/Llama-2-7b-AQLM-2Bit-1x16-hf (9746e511b4eecf972af0a2bb3ebd93f2c5f84ec c).

### J.3 Software Versions

- Rust quantization binary (qam-llm-bench): builds are reproducible from cargo build -release against the included Cargo.toml (see section J.7).
- Python evaluation pipeline (qambench): version 0.1.0, installed via pip install -e qambench[eval].

- transformers version: 4.45.x for the main run; aqlm version installed via pip install aqlm resolves to the latest compatible release at run time.
- lm-evaluation-harness: versions 0.4.11 and 0.4.12 across the study (drift reflects upstream package updates between the cross-model main study and the later Llama-2 extensions; the exact version is recorded per-row in harness.framework\_version).
- torch: 2.4.0+cu121 for the QTIP dequant bridge (section 5.2); the rest of the pipeline runs against whatever torch is installed in the active venv.
- quip-sharp / qtip-kernels: built from the Cornell-RelaxML/qtip repository at the train-fixW forward path; the scripts/day10b\_qtip\_dequant.py script in the companion repo dequantizes QTIP checkpoints to BF16 via the identity-matrix probe described in section 5.2, § “Setup”.

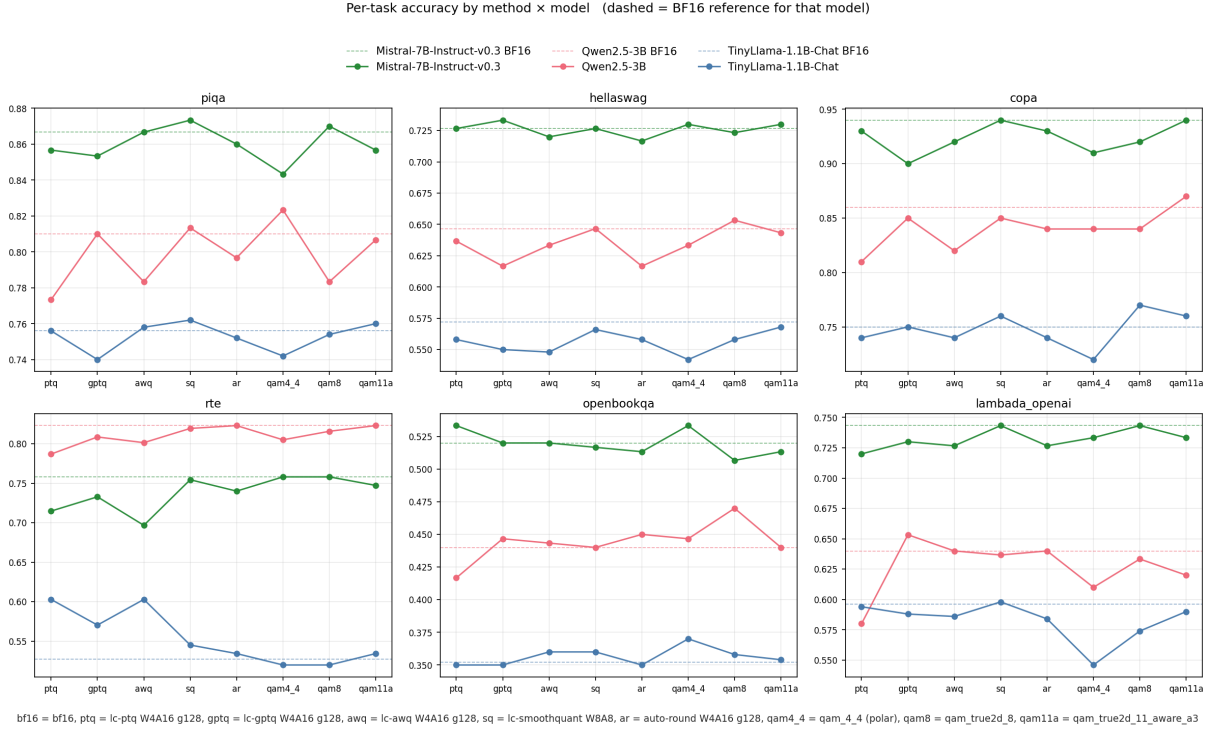


Figure 5: Six-subplot grid (PIQA, HellaSwag, COPA, RTE, OpenBookQA, LAMBADA) with method on the  $x$ -axis and accuracy on the  $y$ -axis. Dashed horizontal lines are the BF16 reference per model. LAMBADA is the most quantization-sensitive task; PIQA and COPA are nearly flat across methods. Method ranking is stable across all six tasks within each model.

## J.4 Hardware

Every row in the paper was produced on a single NVIDIA A100 80 GB on a rented Vast.ai host. The total GPU time consumed across the study — including cross-model main run, Stage D, multi-seed, per-layer diagnostic, prop:aware A1 empirical check, MMLU, Llama-2-7B frontier comparison (including QTIP dequant), and Llama-2-13B scale extension — is approximately 20 A100-hours. The total Vast.ai cost at the host’s hourly rate was approximately USD 34.

## J.5 Per-Method Hyperparameters

Reported in section 5 § “Configurations” and table 7, table 2, table 1, etc., per method. Concretely:

- RTN / GPTQ / AWQ / AutoRound: *W4A16* group size  $g = 128$ , symmetric, f16 per-group scales. AutoRound runs 200 SignSGD iterations.
- SmoothQuant: *W8A8*, smoothing strength  $\alpha_{sq} = 0.5$ , 128 calibration sequences.
- QAM-W: see section 3. Block-Hadamard block size  $b = \min(2^{\lceil \log_2 d_{in} \rceil}, 1024)$ .

Activation-aware exponent  $\alpha = 0.3$ , clamped to  $[1/16, 16]$ , geometric-mean normalized to 1 (section B).

- AQLM 2-bit  $1 \times 16$ : published checkpoint; `in_group_size` = 8, `nbits_per_codebook` = 16, `num_codebooks` = 1.
- QTIP-4Bit / QTIP-2Bit: published checkpoint; trellis  $L = 16$ ,  $K \in \{4, 2\}$ ,  $V = 2$  (per QTIP authors’ release).

## J.6 Determinism

Per-row PPL and KL are deterministic given the manifest’s `weights_sha256` hash, the corpus SHA-256, the eval-time `torch.float16` dtype, and the harness version. The  $\Delta$ PPL% spread across stride-window starting offsets is reported in table 8 on three offsets  $\{0, 4000, 8000\}$  for two headline configurations on each instruction-tuned model. The  $\Delta$ PPL% std observed there is 0.03–0.08 percentage points, which is the noise floor for the cross-model rows.

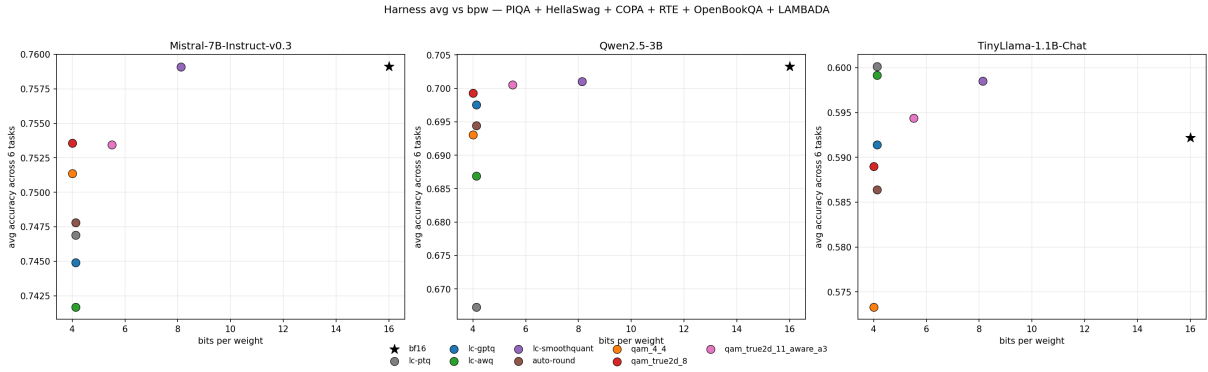


Figure 6: Bits-per-weight vs. harness average across the six-task panel, one panel per model. The shape mirrors the PPL slope in fig. 2: the harness story confirms the WikiText-2 story.

Table 12: TinyLlama-1.1B-Chat per-task harness accuracy at limit=500.

config	avg $\uparrow$	COPA $\uparrow$	HellaSwag $\uparrow$	LAMBADA $\uparrow$	OBQA $\uparrow$	PIQA $\uparrow$	RTE $\uparrow$
BF16 (ref)	0.5922	0.7500	0.5720	0.5960	0.3520	0.7560	0.5271
SmoothQuant	0.5985	0.7600	0.5660	0.5980	0.3600	0.7620	0.5451
★ QAM-W-5.5	0.5944	0.7600	0.5680	0.5900	0.3540	0.7600	0.5343
GPTQ	0.5914	0.7500	0.5500	0.5880	0.3500	0.7400	0.5704
AutoRound	0.5864	0.7400	0.5580	0.5840	0.3500	0.7520	0.5343
AWQ	0.5991	0.7400	0.5480	0.5860	0.3600	0.7580	0.6029
★ QAM-W-4	0.5890	0.7700	0.5580	0.5740	0.3580	0.7540	0.5199
RTN	0.6001	0.7400	0.5580	0.5940	0.3500	0.7560	0.6029
★ QAM-W-polar	0.5733	0.7200	0.5420	0.5460	0.3700	0.7420	0.5199

## J.7 Code Release

The companion code, anonymized for review, is available at <https://github.com/white07S/qam-w> and contains:

- The Rust qam-codec library and qam-llm-bench CLI binary.
- The Python qambench package (loaders, perplexity, KL, lm-evaluation-harness adapter).
- Per-experiment scripts under scripts/ that exactly reproduce each results directory:
  - run\_cross\_model\_main.sh (cross-model main study),
  - run\_mlp\_attention\_mistral.sh (Stage D Mistral),
  - run\_multiseed\_and\_lowbit\_fill.sh (multi-seed + 3.5 bpw Mistral fill),
  - analyze\_layer\_output\_identity.py (Prop. B.1 anchor),
  - run\_mmlu\_panel.sh (MMLU),
  - check\_activation\_aware\_assumption.py (Prop. 1 A1 check),
  - run\_llama2\_7b\_frontier.sh

(Llama-2-7B + AQLM frontier), dequant\_qtip\_checkpoint.py (QTIP loader bridge), run\_llama2\_13b\_scale.sh (Llama-2-13B scale).

- Reduce scripts that render the LaTeX rows of each table from the raw eval JSONs: reduce\_results\_to\_tables.py (Stage D, multi-seed, low-bit fill).
- Plot scripts in scripts/make\_plots.py and scripts/plot\_kl\_vs\_dppl.py.
- A Dockerfile and Makefile (make run) that build the full Rust + Python environment for one-command end-to-end reproduction.

The repository is provided under a proprietary, all-rights-reserved license (see LICENSE in the companion repo).

Table 13: Qwen2.5-3B-Instruct per-task harness accuracy at limit=300.

config	avg $\uparrow$	COPA $\uparrow$	HellaSwag $\uparrow$	LAMBADA $\uparrow$	OBQA $\uparrow$	PIQA $\uparrow$	RTE $\uparrow$
BF16 (ref)	0.7033	0.8600	0.6467	0.6400	0.4400	0.8100	0.8231
SmoothQuant	0.7010	0.8500	0.6467	0.6367	0.4400	0.8133	0.8195
*QAM-W-5.5	0.7005	0.8700	0.6433	0.6200	0.4400	0.8067	0.8231
GPTQ	0.6976	0.8500	0.6167	0.6533	0.4467	0.8100	0.8087
*QAM-W-4	0.6993	0.8400	0.6533	0.6333	0.4700	0.7833	0.8159
AutoRound	0.6944	0.8400	0.6167	0.6400	0.4500	0.7967	0.8231
AWQ	0.6869	0.8200	0.6333	0.6400	0.4433	0.7833	0.8014
*QAM-W-polar	0.6931	0.8400	0.6333	0.6100	0.4467	0.8233	0.8051
RTN	0.6673	0.8100	0.6367	0.5800	0.4167	0.7733	0.7870

Table 14: Mistral-7B-Instruct-v0.3 per-task harness accuracy at limit=300.

config	avg $\uparrow$	COPA $\uparrow$	HellaSwag $\uparrow$	LAMBADA $\uparrow$	OBQA $\uparrow$	PIQA $\uparrow$	RTE $\uparrow$
BF16 (ref)	0.7591	0.9400	0.7267	0.7433	0.5200	0.8667	0.7581
SmoothQuant	0.7591	0.9400	0.7267	0.7433	0.5167	0.8733	0.7545
*QAM-W-5.5	0.7534	0.9400	0.7300	0.7333	0.5133	0.8567	0.7473
GPTQ	0.7449	0.9000	0.7333	0.7300	0.5200	0.8533	0.7329
AutoRound	0.7478	0.9300	0.7167	0.7267	0.5133	0.8600	0.7401
AWQ	0.7417	0.9200	0.7200	0.7267	0.5200	0.8667	0.6968
RTN	0.7469	0.9300	0.7267	0.7200	0.5333	0.8567	0.7148
*QAM-W-4	0.7536	0.9200	0.7233	0.7433	0.5067	0.8700	0.7581
*QAM-W-polar	0.7514	0.9100	0.7300	0.7333	0.5333	0.8433	0.7581